CHARACTERIZATION AND ENHANCEMENT OF FATIGUE AND FRACTURE PROPERTIES IN THERMOPLASTIC FFF PARTS USING IN-SITU ANNEALING

by

Manjarik Mrinal

DISSERTATION

Submitted in partial fulfillment of the requirements

for the degree of Doctor of Philosophy in Mechanical Engineering at

The University of Texas at Arlington

December, 2021

Committee Chairman: Dr. Robert Taylor

Supervising Committee:

Dr. Ankur Jain

Dr. Ashfaq Adnan

Dr. Victoria Chen

Dr. Amir Ameri

ABSTRACT

CHARACTERIZATION AND ENHANCEMENT OF FATIGUE AND FRACTURE PROPERTIES IN THERMOPLASTIC FFF PARTS USING IN-SITU ANNEALING

Manjarik Mrinal, Ph.D.

The University of Texas at Arlington, 2021

Fused filament fabrication (FFF) show high anisotropy and reduced mechanical properties as compared to conventional manufacturing techniques. This happens due to the poor interlaminar bonding between the layers, as a result of premature halt of bond healing process. Previous research works show multiple approaches to improve the bond quality to enhance the mechanical properties of FFF parts, however these are complex and expensive techniques. In this work a novel print head assembly is presented to offer a simple and effective solution by applying a thermal field to the part as it is being printed to preheat the previously deposited layer, thus improving the interlaminar bonds and eventually the mechanical properties of the parts. This assembly is compatible with most of the commercial FFF printers with no major modification, unlike other existing technologies. An optimized print head assembly was developed to improve the Fatigue and Fracture properties of FFF parts while minimizing the mass of the block to provide maximum enhancement of the properties while reducing geometric distortions. A design of experiments approach has been used to identify the main effects and interaction effects between the two factors (Plate Thickness and Nozzle Height) with three levels each for five response variables (Increase in Number of Cycles to Failure, Increase in Fracture Toughness, Decrease in Width, Increase in Thickness and Increase in Skewness). The DOE shows that the nozzle height and plate thickness main effects are present for all response variables. A localized cooling mechanism has been

provided to cool the upper sections of the print head to prevent filament softening and save from clogging and print failure. Parts printed with the optimized print head shows good correlation with the DOE analysis with major improvements in mechanical properties and less geometric distortion of the FFF parts. In conjunction, mesostructured analysis of these parts showed a transformation in the void shape from diamond to circular indicating that these voids have much lower stress concentration rather than failure initiation points, supporting the experimental data. Meso-structure analysis of fractured surface was done to understand the change occurring at the failed surfaces.

TABLE OF CONTENTS

CHAPTER 1 . INTRODUCTION **1**

CHAPTER 2 BACKGROUND **5**

2.1 FUNDAMENTAL OF FUSED FILAMENT FABRICATION (FFF) 5
2.2 FATIGUE AND FRACTURE BEHAVIOR IN FFF 6
2.3 GEOMETRIC PROPERTIES PROCESSED BY FFF 11
2.4 MECHANICAL ANISOTROPY OF FFF-PRINTED PARTS AND EXISTING IMPROVEMENT METHODS 12

CHAPTER 3 METHODOLOGY **15**

3.1 PROCESS IMPROVEMENT 15
3.2 TEST PROCEDURE 18
3.3 EXPERIMENTAL PROCEDURE 24

CHAPTER 4 RESULTS AND DISCUSSIONS **26**

4.1 INCREASE IN NUMBER OF CYCLES TO FAILURE, INCREASE IN FRACTURE TOUGHNESS IN FATIGUE, DECREASE IN WIDTH, INCREASE IN THICKNESS AND INCREASE IN SKEWNESS. 26
4.2 INFLUENCE OF IN-SITU ANNEALING ON VOID STRUCTURE AND IT EFFECT ON MECHANICAL PROPERTIES 38
4.3 TWO-WAY FIXED EFFECTS MODEL AND ASSUMPTIONS VERIFICATION. 41
4.4 ANOVA AND FACTOR INTERACTIONS 44
4.5 PAIRWISE COMPARISONS. 50
4.6 OPTIMIZED CONFIGURATION OF NOVEL PRINTHEAD ASSEMBLY 55
4.6.1 Approach to Optimized Configuration *55*
4.6.2 S-N plot of Reference vs Optimized Configuration *57*

CHAPTER 5 CONCLUSION **59**

Chapter 1 . Introduction

Traditional manufacturing techniques have been steadly progressing to facilitate production of complex structures and geometrically accurate parts. Mainly these kind of techniques are subtractive in nature, involves removal of material from stock material to create a desired part, some frequently used methods for instance are: turning, milling and drilling, etc. However, with traditional manufacturing, fabricating complex geometries could cost much more than making simple ones and some designs are not even possible to achieve through theses techniques. In contrary, Additive Manufacturing (AM) as name suggests is an additive process, where parts are manufactured in layer-by-layer manner. It offers the capabilities to produce non-conventional geometries such as topologically optimized, generative designs and functional parts with minimum material wastage [1,2]. AM has shown great promise due to its capability to provide customized and sustainable solutions. [3,4]. The ASTM F42 committee has divided the AM processes into 7 broad categories to obtain standardized terminology. The different AM techniques can be classified as: Material Extrusion (ME), Powder Bed Fusion (PBF), Binder Jetting (BJ), Sheet Lamination (SL), Material Jetting (MJ), Vat photopolymerization (VP) and Direct Energy Deposition (DED) [4]. Each of these techniques have their own special features like material option, speed, resolution and cost, thus offering a wide range of possibilities [5]. Amongst all the AM techniques, the most popular and commonly used technique is Fused Filament Fabrication (FFF) [6]. FFF's popularity can be attributed to its ease of accessibility due to low-cost machines and the availability of a variety of materials commercially [7]. Polymers like polylactic acid (PLA), acrylonitrile butadiene styrene (ABS) [8], polycarbonate (PC) [9], polyether ether ketone (PEEK) [10,11], ULTEM 9085 [12] are the primary feedstock materials used in FFF, also some metal

alloys with low melting temperatures can be used [13]. In FFF, a CAD model is used to fabricate parts in a layer wise fashion as seen in Figure 1. Other AM techniques have an energy source that rasters over either a powder bed or photopolymer causing selective fusion to form the final shape [14-18], whereas in FFF a thermoplastic filament is fed into a heated extruder which deposits the polymer melt through a nozzle at a temperature beyond the glass transition temperature onto a heated build platform [19]. The print nozzle is moved in the x-y plane by a gantry whereas for the out of plane movement the nozzle or bed is moved in the z-direction.

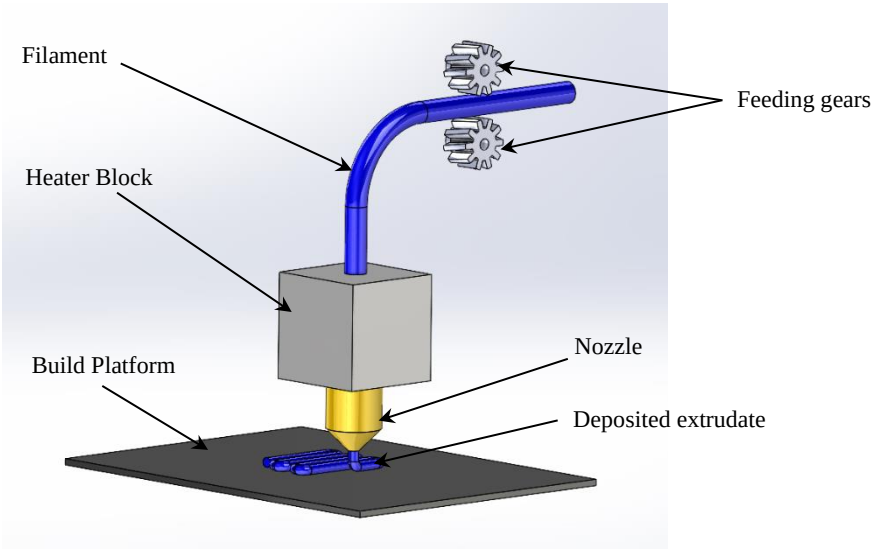

Figure 1. Schematic of the FFF process

In recent times FFF has found its utility in wide range of disciplines, such as : aircraft industry [20,21], biomedical application, like generating scaffolds to facilate tissue growth, dentistry [22-24], complex lattice structure and hybrid materials [25-27], 3D printing batteries [28] and in addition to the aforementioned, 3D printing its own components [29]. FFF has a plethora of applications, thus, the characterization and improvement of its mechanical properties, has become critical. It is seen that parts fabricated using FFF suffer from a major drawback of reduced

mechanical properties [30-32] and are highly anisotropic as compared to their injection molding counterparts and thus cannot be directly used in engineering applications. These reduced mechanical properties and anisotropy of FFF parts limit their use majorly for prototyping and not for the fabrication of end use parts. Thus, to tap into the advantages provided by FFF it is of vital importance to study the parameters that affect the mechanical properties and methods employed to improve these properties.

Studies have shown that the interlaminar bond between the polymer layers dictates the mechanical properties of FFF parts. The interlaminar bond formation in FFF parts has been modeled and described in multiple ways based on polymer interface healing, with the main stages being [33-36]: (1) Heating of the Filament-Filament interface above the glass transition temperature, Tg enabling polymer flow and mobility; (2) Intimate physical contact between the adjacent polymer interfaces (adjacent layers in FFF parts); (3) Thermal polymer healing or diffusion at the interface (4) Cooling of the interface below Tg. Thus, in the FFF process a polymer melt is extruded onto a previously deposited comparatively cooler layer causing the interface to rise initially and then fall rapidly below Tg. The interlaminar regions (weld region) between adjacent filaments are the weakest sections in FFF parts due to this complex thermal history thus leading to premature failures [36]. It is also seen that due to the rounded nature of the deposited polymer melt the presence of voids is an inherent defect of FFF parts thus further degrading their mechanical properties [37-40]. FFF parts have been studied under multiple test conditions like tension [41-45], compression [46-50], fracture [51-55], torsion [38,56] and dynamic loading [57-60] reinforcing the dominant effect of the weak interlaminar bonds on the overall mechanical properties of FFF parts.

Comprehension of the strength required to bear a certain type of load condition is crucial for any such applications mentioned above [61, 62]. A structure could fail due to fatigue condition, thus it is important to understand it's resistance to cyclic loading and unloading [63]. Cumulative stress accumulation and permanent structural damage could occur due to fatigue condition. This could result in fracture of the part after certain repeated cycles. Generic polymers are prone to fatigue failure below their yield strength, microfractures and failure could occur under such loading condition [64]. Therefore, it is critical to understand the fatigue behavior of AM polymer parts. In this study we have focused on the work done on fatigue life of 3D printed FFF parts and as well as area that needs to be explored and suggested future work.

Thus, an improvement in the interlaminar bond strength is warranted if FFF parts are to be used for end use applications. In the current work, a print head has been designed such that there is an significant improvement in the mechanical properties. A nozzle with an integrated plate is used which applies a passive thermal load onto the previously printed layers, thus keeping the deposited layers above the glass transition temperature leading to improved bond formation. Thermal load also causes geometric distortion; thus, characterization of geometric distortion is also performed to understand the distortion associated with degree of in-situ annealing. The print head geometry (plate thickness and nozzle height) are optimized by analyzing the factor effects using a design of experiments approach. Further a study of the changes in the void structure is done to better understand the improvement in mechanical properties.

Chapter 2 Background

2.1 Fundamental of Fused Filament Fabrication (FFF)

A three-dimensional geometric part is designed using CAD in the Fused Filament Fabrication process. Typically, a filament is fed and melted in liquefier before a nozzle deposit it on the build platform in a FFF process as shown in Figure 1. This section provides primary introduction about FFF process. In order to produce parts by Additive Manufacturing process, a CAD model is converted to a machine compliant format which usually is stereolithographic (STL) and 3D manufacturing format (3MF). Further in the slicing step, 3D model is transformed into printable format, where the model is dicretezised in multiple layers. In practical, this 3D model is built or printed by depositions layers on top of each other. G-Code, a programming language that controls the motion of FFF extruder for each layer during deposition process in X-Y plane. Most commercial FFF machines have inbuilt slicing and G-coding software included where STL files is to be directly uploaded to machine software. Build orientation, print speed, and infill density values are provided into order to setup machine before printing process is initiated, this step is commonly known as machine setup. Generally, a pre-generated tool path directs extruder movement in a horizontal plane for depositing layers in FFF printers. Upon delivering a layer, the build platform then moves in z-direction. Every new layer is deposited on top of the previously deposited layer until printing process is accomplished. These consecutive layers and their adhesion governs the strength of built parts. In order to achieve a quality adhesion between previous layer and the new incoming layer being deposited, it is required to provide subtantial amount of energy to actuate the prior deposited layer, yielding adhesion between the layers.

2.2 Fatigue and Fracture behavior in FFF

Fatigue:

Use of polymers have grown significantly not long ago, especially in engineering field, this has caused a surge in the demand of engineering grade polymers and their behavior. This has led to the need of exploring the behavior of such materials under fatigue loading condition, which happens to resembles the real condition it would suffer being out there in service. The fatigue loading is a cyclic loading condition where the stress levels are much lower than the level they could withstand in static loading. In static loading, failure occurs at a higher stress level, however in fluctuating loads, polymers could fail at much lower level of stress. Therefore, it has caused the urge to understand, how the polymers resist failure and investigate the technologies that could help in improving the performance of these polymeric materials in fatigue condition. It is fairly intricate process to understand as there are numerous important factors that can influence such as stress intensity, alternating stress amplitude, frequency, surface condition, frequency and environmental condition. Also, there are factors associated to material properties, i.e., viscoelastic nature, molecular weight and polymer structure. There has been numerous works published related to the fatigue behavior in elastomers and thermoplastics [64, 65], and composites and fibers [66-69]. Fatigue analysis in FFF still remains untarnished, however some investigations have been done and, in this work, review of such literatures will be in focus along with the background information on fatigue in polymers.

It is seen to have polymers being more vulnerable to alternating load in comparison to metal due to their viscoelastic nature and poor thermal conductivity. In polymers failure could also occur because of heat generation within the part, it may melt and rupture owning to heat generation.

Fatigue damage experienced by a structure lies within elastic limit (i.e., high cycle loading) or in elastic plus plastic range of the material (low cyclic loading). Fatigue failure of polymers could be bifurcated in two cases [70,71], due to thermal failure or mechanical failure.

2.2.1 Thermal fatigue in polymers

When polymers are exposed to cyclic loading, they dissipate some energy in every cycle because of their viscoelastic nature. This results in heat generation within the part and rise in temperature, which is equal to the heat dissipated [72,73]. During testing the temperature of the specimen may rise to the glass transition temperature T_g, or may stabilize at some other temperature [74]; this would be dependent on the frequency of test, its amplitude, ambient temperature, internal friction and thermal conductivity of the material. Fatigue failure originated due to the presence of thermal effect is not considered as a natural response of the material in such loading conditions. The part rather fails in ductile manner and quickly [75-76], it is likely to be referred to be in low cycle regime.

2.2.2. Mechanical fatigue in polymers

In case of metals, when they undergo cyclic loading, they experience cyclic softening or cyclic hardening, depending upon if the metal was soft or hard initially. Whereas in the case of polymers it is not exactly the same, when they are exposed to cyclic strain, they rather exhibits cyclic softening, although at the same time is also dependent upon the polymeric structure [77].

During fatigue testing mechanical failure occurs mostly at the in-between value of the oscillating stress and it starts with crack initiation and then proceeds with crack propagation, eventually leads to a complete fracture. In such tests, generally crack initiation begins at a surface

defect or stress concentration zone, in unnotched specimens. Surface crazing and plastic deformation is observed at the initiation point. Mechanical fatigue failure happens to have higher fatigue life due to the low stress levels and low frequency of the test, also frequently called as high cycle fatigue. In this regime the polymers expresses quite brittle behavior [78-79]. In the event of notched specimens, failure then happens at the crack tip because of the fracture of lamina or fissure [80]. Here crazing is seen at the crack tip. If the test is performed at very low stress level, then it is possible the specimen would not even fail up to or beyond10^7 cycles, this is called as Endurance limit.

Fracture Mechanics:

The objective of this study it is to concentrate on the crack initiation and crack propagation, which occurs during cyclic loading. Like in previous section, fracture in fatigue takes place during alternating loading condition, at some kind of stress concentration zone where crazing originates. Thereafter the region experiences plastic deformation and subsequent formation of microcracks in the region. Under cyclic loading, the crack propagates combining the microcracks and forming a larger crack. Once a critical size of the crack is reached, a sudden fracture or catastrophic fracture takes place.

Fracture Mechanics is mainly split into two kinds: Linear Elastic Fracture Mechanics and Elastic–Plastic Fracture Mechanics. They have been discussed briefly below to understand the mechanics of tests conducted.

2.2.3 Linear Elastic Fracture Mechanics (LEFM)

In LEFM, when a well-defined fracture specimen is tested under a loading condition, crack extension occurs when the resistance to crack extension of the material is surpassed by the strain energy release rate per unit area. It is critical to have the plasticity around the crack tip to be proportionately small, to fulfil the assumptions associated with LEFM. K is a stress intensity factor. However, when a specimen is tested in mode I condition, the stress intensity factor becomes K_I, specific to mode I and it can be expressed as in equation 1,

$$K_1 = Y\sigma\sqrt{\pi a} \quad [1]$$

where a is the crack length, σ is the stress applied and Y is the specimen geometry. Similarly, for other crack opening modes, i.e., mode II and III, as in figure 2, respective expressions could be derived. The conditions could be plain stress or plain strain, depending on the geometry of the specimen, thinner the specimen it moves towards plain stress condition whereas for thicker geometry it follows plain strain condition. In plain stress condition the value of the stress intensity factor could be overestimated, whereas in plain strain condition we get a conservative value of K. Thus, when a linear elastic specimen is tested in mode I and the critical value of its inherent crack resistance is denoted as K_{Ic}, respectively.

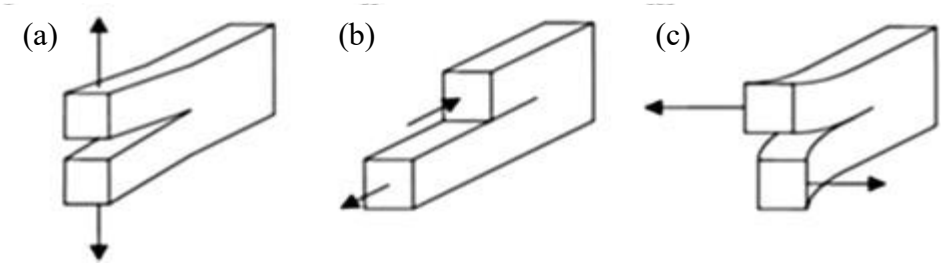

Figure 2: Pictures showing different modes of crack-opening, [81]

Mode I is the most commonly used mode, as it is relatively straight forward to execute the test for all the types of fracture specimens as shown in figure 3. Although, the other crack-opening modes are significant as well and in certain conditions they are opted over or along with mode I, for instance in case of composites.

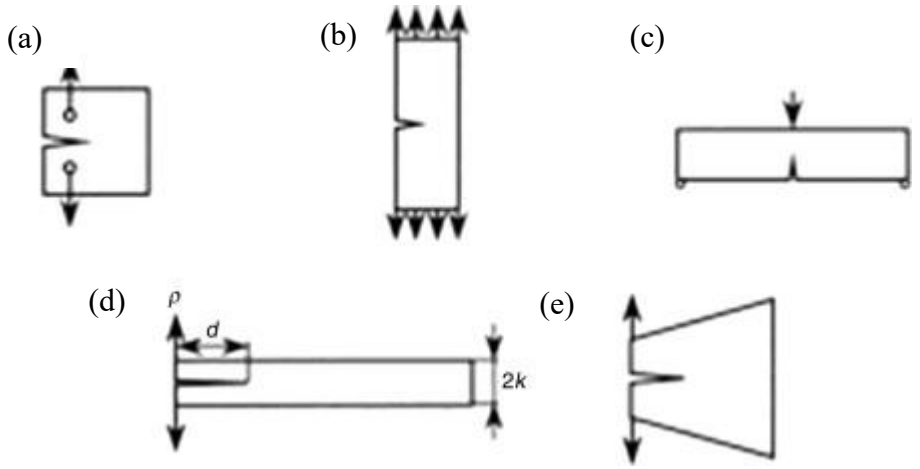

Figure 3: Pictures of different specimen geometries for mode I fracture toughness testing of plastics: (a) Compact tension (CT); (b) single-edge-notched tension (SENT); (c) single-edge-notched bending (SENB); (d) double cantilever beam (DCB); and (e) tapered double cantilever beam (TDCB), [81].

It is a significant consideration while performing these tests, is the preparation of the specimen. In-order to yield a valid testing result the specimens must have a sharp pre-crack. Usually, such sharp cracks are induced using sharp razor blade and passing it through the machined or predesigned notch. However, it is a tricky procedure, and much be performed carefully to

prevent any residual stress generation, as polymers have the tendency to undergo ductile yielding and might infirm the obtained results.

2.2.4 Elastic–Plastic Fracture Mechanics (EPFM)

If the plastic shows brittle behavior, LEFM is valid in this realm. Although if thermosets or thermoplastics tend to exhibit high degree of crazing then EPFM become applicable. When fracture specimens of toughened and engineering grade plastics are tested, they show excessive nonlinear stress-strain curves because of the immoderate presence of plasticity at the crack tip. This excessive plasticity leads to ductile fracture rather than unstable sudden fracture. Therefore, it instigated the need of theory that could describe the excessive plastic deformation during crack growth and offer methods for testing fracture specimens that doe does not belong to LEFM, rather it is valid in EPFM.

2.3 Geometric Properties Processed by FFF

Fused Filament Fabrication (FFF) technology is now being used to manufacture prototypes and finished products with magnificent mechanical properties. In the beginning this technology was limited to manufacturing of prototypes. Crucial aspects for assembly and durability such as dimensional, geometric precision and surface finish are drawbacks of this technology. Geometric precisions are unable to match optimum levels acquired by conventional manufacturing processes to greater extend. Printer settings, material properties of cured layers, mechanical efficiency of the 3D printer itself affect quality of printed product. A low cost FFF 3D printer often delivers poor quality components in terms of its mechanical properties and with respect to the machine’s physical capacity to function which directly affects quality if finish

product. Various factors such as thickness of layers, feed rate, movements of extruder and its dimensional accuracy, build orientation, flatness, surface texture play a vital role in FFF 3D printing. All these factors have a direct effect on the printed product and its properties. Thinner the layer, lower the dimensional variation. Extruder feed rate had minimal influence on thinner layers with respect to dimensional accuracy whereas flatness and surface texture are directly affected due to layer thickness and feed rate. It is critical to achieve optimum print quality by optimizing print setting to obtain functional components.

2.4 Mechanical Anisotropy of FFF-printed parts and Existing Improvement Methods

Previous studies make it clear that improving the interlaminar bonding causes the FFF parts to exhibit enhanced mechanical properties. Multiple models have been developed to explain the factors that influence the interlaminar bonding with most models based on the Reptation theory of polymers [34-36,82]. An ideal condition of bonding between two polymeric interfaces is when both interfaces are heated beyond Tg, while the surfaces have intimate contact between. Healing of a polymer interface via molecular interdiffusion is a temperature-dependent process. Interfacial bond strength is dependent on the distance of diffusion of polymer chains across the polymer interfaces and length of their chain. The interpenetration distance (χ) and length of polymer chain (l) can be predicted using the De Gennes Reptation theory. After a period of time, when $t > 0$, The chain ends crosses the boundary of individual bead until complete intermingling of the polymer chains take place at at a reptation time $t = t_r$, after the reptation time the polymer chains fully develop and property of the bond interface approaches that of bulk material. Thus, the polymer chains continues to diffuse till the interface is indistinct and the interpenetration distance (χ)

becomes (χ_{bulk}) equivalent to that of the bulk material at t_r. Similarly, the length of polymer chain grows from (l) at $t > 0$ to (L) at $t = t_r$. Figure 4 shows the schematic of the healing process.

Now the interpenetration distance and length of polymer chain at time t_w have values χ_w and l_w respectively, where t_w is the weld time and lies in between $0 < t < t_w < t_r$. From the work done by Prager et al the healing process is described using a ratio of interface bond strength σ_{bond} and strength of bulk material σ_{bulk}. This ratio is called the degree of healing (D_h) and characterizes the bond strength developed [83]. Equation 2 shows the relation between degree of healing and the different parameters defined previously.

$$D_h = \frac{\sigma_{bond}}{\sigma_{bulk}} = \frac{\chi}{\chi_w} = \left(\frac{l}{l_w}\right)^{\frac{1}{2}} = \left(\frac{t}{t_w}\right)^{\frac{1}{4}} \quad (2)$$

And t_w was found out by Pitchumani et al by empirically fitting an Arrhenius Energy relation [84] given by:

$$t_w = A\, exp\left[\frac{E}{R}\left(\frac{1}{T} - \frac{1}{T_{ref}}\right)\right] \quad (3)$$

Where A is a constant for fitting, E is the Activation energy, R is the Universal Gas constant and T_{ref} is the reference temperature. These studies provide us with parameters that affect the interfacial bonds between polymers during the healing and diffusion process. Studies by Tirrell et al and Lee et al show that the self- diffusion of the polymer chains during the healing process is dependent on the molecular weight (M) given by [85-86]:

$$D = M^{-2} \quad (4)$$

Where D is the coefficient of self-diffusion of the polymer chains. It has also been analyzed that the molecular weight (M) of the polymer chains play a vital role in the interdiffusion process. For very long polymer chains where $M >> Mc$, which is the critical molecular weight of entanglement the maximum bond strength σ_∞ can be achieved at weld time t_w instead of the reptation time t_r.

Further studies regarding the coefficient of self-diffusion show that it is inversely proportional to the viscosity of the polymer melt [87-89]. A higher coefficient of self-diffusion signifies better interfacial bonding during the healing process.

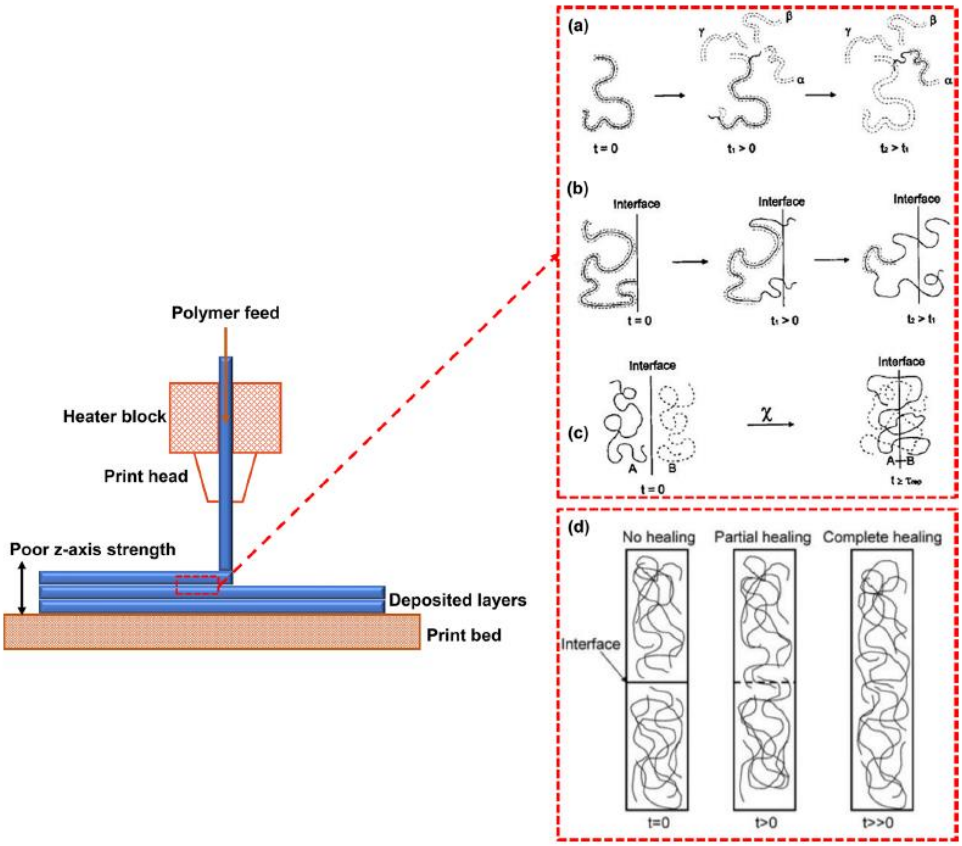

Figure 4. Healing process between two polymer surfaces maintained in intimate contact, [90].

Thus, it is clear that FFF parts show substantially reduced mechanical properties as compared to conventional manufacturing techniques, and these mechanical properties are dominated by the weld lines and inter-laminar bonds between adjacent layers. The above mathematical models provide us with parameters that can be optimized to improve these interfacial bonds which are the weakest sections in FFF parts.

Chapter 3 Methodology

3.1 Process Improvement

From the literature survey it has been seen that the complex temperature distribution around the deposited polymer melt combined with heat transfer between adjacent filaments determines the quality of bond [91,92]. Furthermore, work has been done on different in-situ [93-96] and post processes [97-99] to improve mechanical properties in FFF parts. Previous work on post-process thermal annealing has shown to increase the inter-laminar bonding by heating the part well beyond its glass transition temperature resulting in significant increase in the mechanical strength of the parts [100-102]. These method does lead to a substantial increase in strength, but the geometric accuracy of the part is compromised. Also, applying a post -process thermal load increases the total build time of the final part. In-situ approaches have been studied which provide an external heating source to facilitate inter-laminar bonding and these methods have shown great promise[93-96]. Microwave heating has been used to raise the local temperature during the fabrication of FFF parts [103]. In another study, a complex setup of different optics, mirrors, and a near- infrared laser beam was used to focus the beam on the part to locally raise the temperature before depositing the polymer melt. But these approaches utilize complicated, expensive, and additional equipment further complicating the FFF process. Study was done by Ravoori et al [96], where a rectangular metal block was attached to the nozzle assembly to apply an in-situ thermal load and thus increasing the neck growth. This provided a comparatively simple and cost-effective solution to increasing the inter-laminar bonding by in-situ heating. But this work did not analyze the effect of the thickness of the block and the height of the nozzle from the block on the mechanical strength of the parts. Also, previous studies, [104-107] have shown that inter- laminar bonds are the weakest along the out-of-plane or z-direction due to the reduced reptation and neck

formation seen, when a hot polymer melt is extruded onto a layer that has already cooled down. But in the work done by Ravoori et al [96], the tensile coupons printed were not oriented with their length along the out-of-plane direction rather they were laid flat onto the bed. Further, more work done Rane et al [108] to charaterise the effect of nozzle height and plate thickness on ultimate tensile strength and fracture toughness. In the work the specimens were printed along z direction, standing upright on the bed, thus providing an accurate representation of the neck growth phenomenon between two consecutive layers. In this prior study also tests were conducted in monotonic loading, fatigue performance and geometric distortion were not characterized, as well as did not provide the understanding of the trade off between enhanced mechanical properties and geometric distortion..

In the current work, a print head assembly was designed in collaboration with Rane, to apply an in-situ thermal load while the part is being printed as shown in figure 5. A novel printhead assembly is designed with a circular nozzle installed into the heated liquefier. The key features of this setup is that, it has a completely novel nozzle design which consists of an integrated disc like plate, the issue experienced with the pervious design in [96], of not being able to print tall parts is solved by adding a localized cooling fan, it does not required any external heating source since the nozzle is coupled with the heater block and it happens to be an effective technology to enhance mechanical properties, while being simplistic and inexpensive unlike other systems.Two factors namely block thickness and nozzle height from block are studied each factor with 3 levels. A design of experiments (DOE) is performed using a two-way full factorial analysis to study and characterize fatigue, fracture toughness and geometric distortion and obtain a statistical model. Analysis of Variance (ANOVA) is conducted to test the significance of each factor on the increase

in fatigue, fracture toughness and change in geometric distortion to find the optimum value from the different combinations. Further characterization of the change in the cross-sectional area is done to see how the modified heater block assembly affects the geometric accuracy of the parts. Changes in the characteristic long voids seen between adjacent rasters and cross-sectional images were analyzed. This study provides a detailed analysis of the contribution of different factors of the novel printhead assembly which conducts the studies on fatigue, fracture toughness properties and geometric distortion .

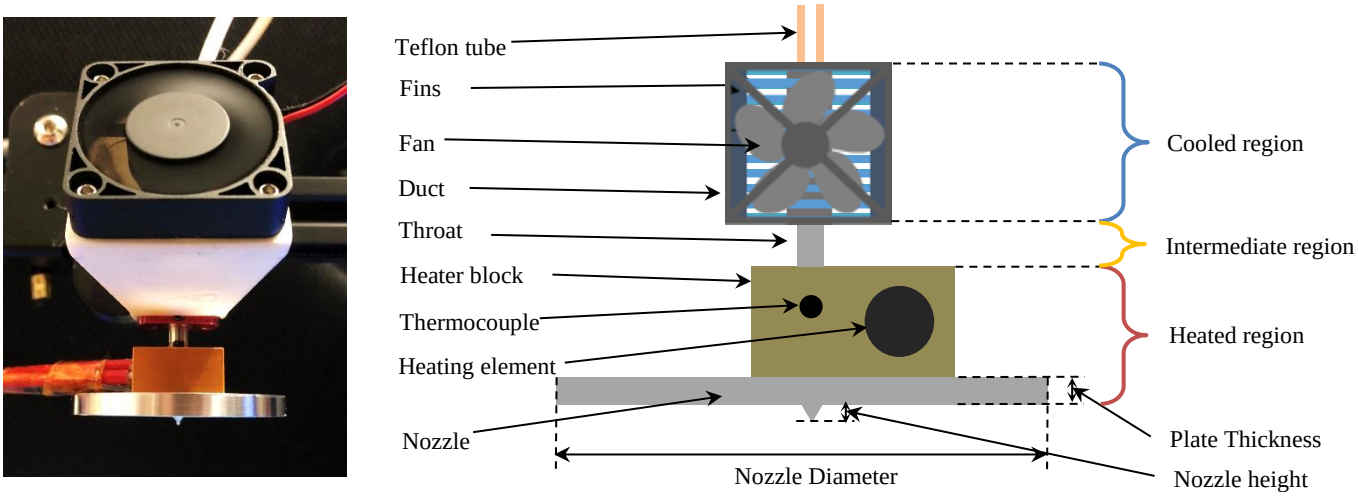

Figure 5. Novel print head assembly and its schematic

3.2 Test Procedure

In this study Polylactic Acid (PLA) filament (Hatchbox 3D, Pomona, CA, USA) of 1.75 mm diameter was used to generate test coupon. There were three kind of tests coupons, for fatigue test coupons, dogbones were printed based on ASTM D638-02a standards as shown in Figure 4 and the compact tension (CT) specimen were printed using ASTM D5045-99. Rectangular bar test coupon was designed to characterize the geometric changes. The test coupons were designed on SOLIDWORKS 2016 (Dassault Systems, Waltham, MA, USA) and later converted into G-Code by using Simplify3D software. The test specimens are seen printing in the figure 6 with the experimental setup consisting of Creality Ender 3 Pro printer and the attached novel print head assembly. The prints were made with a 0.4 mm brass nozzle and bed temperature were kept at 200˚C and 60˚C respectively. The specimens were 100% filled with no perimeter shells to avoid introduction of any other raster direction. These print settings were based on the previous study to provide good print quality, strength and reduced print times. The dogbone samples were printed standing upright in z-direction as seen in figure 6. This was done to achieve an accurate representation of the weak inter-laminar bonds between two adjacent layers and therefore provide absolute results for increase in fatigue life for the weakest inter-laminar bonds. In case of Fracture testing, CT specimen were printed such that the crack plane was parallel to the layers to characterize the interlayer plain stain fracture toughness (K_{Ic}) as shown in Figure 6. To print the CT specimen with a pre-cracked zone, a specific procedure was followed. An alarm was inserted in the G-code to indicate that half the number of layers have been printed. Once this alarm went off a fixture was used to insert a Kapton tape which forms the sharp pre-crack in the CT specimen. The infill raster angle was kept at 0 same as case of dogbone specimen.

The circular aluminum nozzle had fixed plate diameter of 50 mm. The plate thickness had 3 levels: 2mm, 5mm and 10 mm and the nozzle height from the block was adjusted to 3 levels: 1mm, 1.5mm and 2mm. A cooling fan with a duct was provided for localized cooling above the heated liquefier region as seen in the Figure 7. Preliminary study showed that the heat is generated in the upper section (cooled region) due to the heat travels upwards via conduction and convection leading to softening of the filament in the upper sections of the extrusion chamber causing print failure after printing some layers.

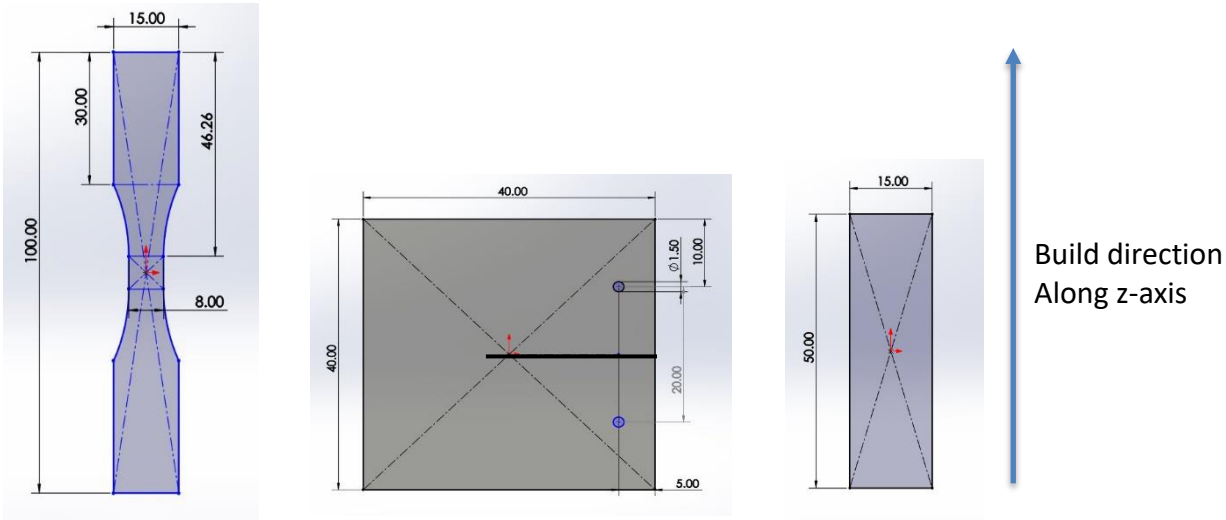

Dogbone Specimen

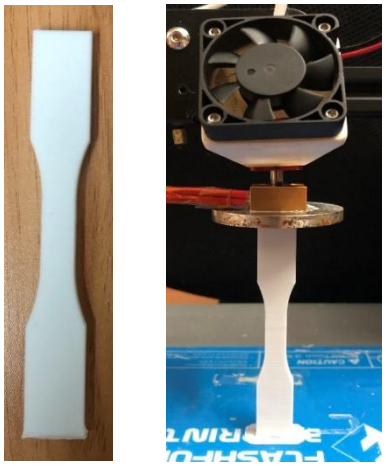

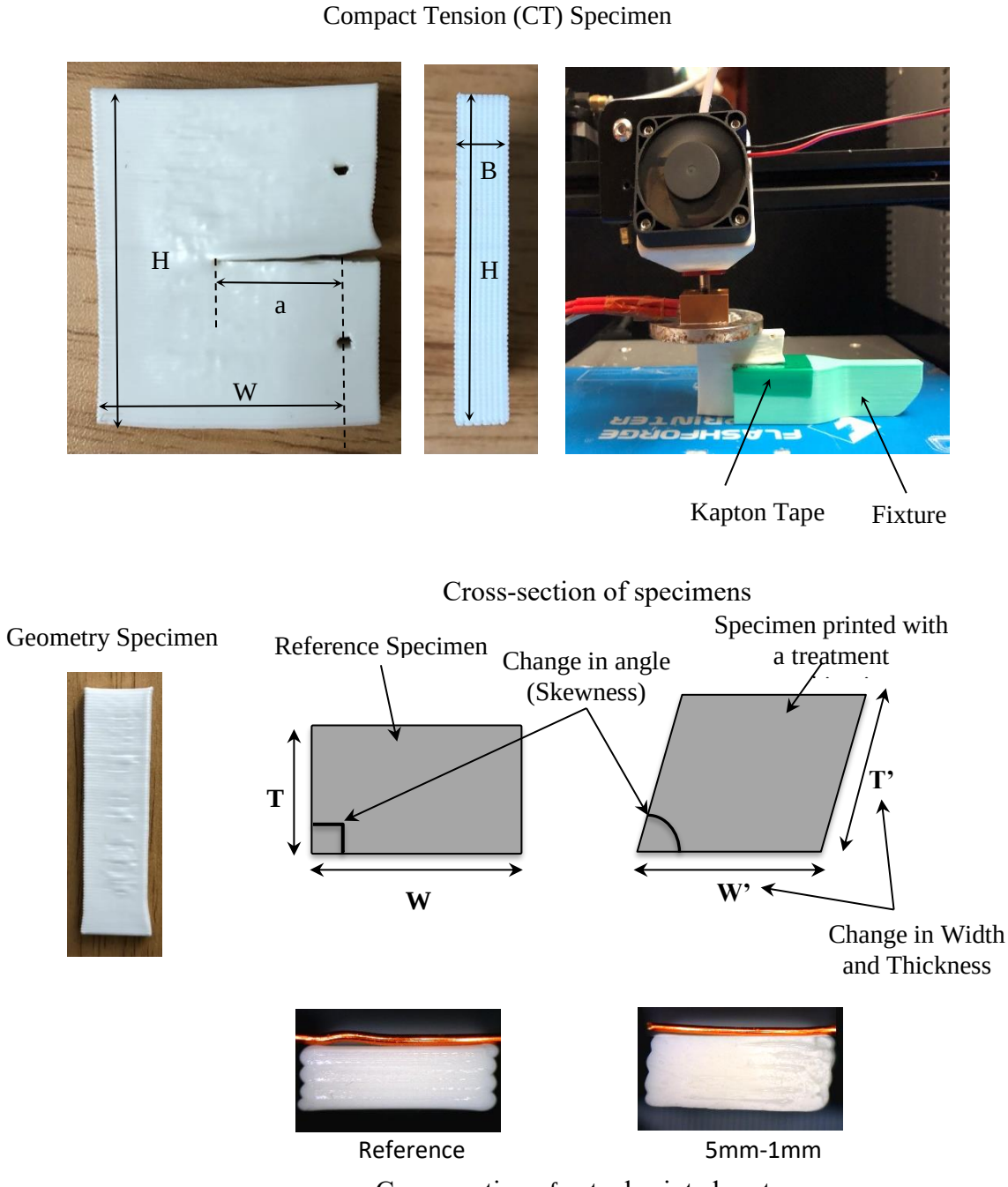

Figure 6. Fabrication of fatigue, fracture and geometry specimen

Standard hot ends provide fans to cool the part being printed as well as the upper sections of the extrusion chamber but using these attachments result in the heater block to be continuously cooled leading to extended wait times in heating up the heater block and thermal runaway errors in the printer. Thus, using the focused cooling mechanism solves the issues discussed. The simulations show that the temperature in the throat is much higher for the assembly without a fan whereas the temperature in the throat falls below the glass transition temperature of PLA when a fan is used. FFF systems require the filament to maintain its structural integrity before entering the heated liquefier to act as a piston and push out the polymer melt through the nozzle, which is achieved by using the localized cooling mechanism.

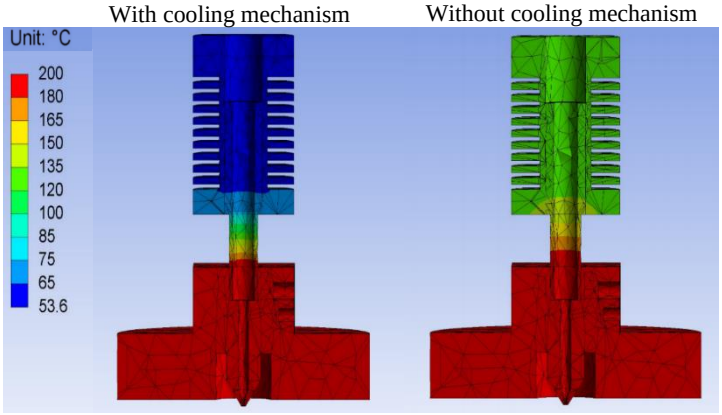

Figure 7. Cooling mechanism for localized cooling above the heated liquefier, [89]

Replications were generated for each part by printing them separately to avoid compounding error for different factor levels. Both the fatigue and fracture specimens were then tested under fatigue loading using a Shimadzu Tensile Testing machine. To apply the cyclic loading condition to fatigue specimen lower stress and upper stress level were set as 10% and 90% of average Ultimate tensile Strength (UTS) of 15 control specimens tested under monotonic loading. For fracture

specimens lower load and upper load level were set as 10% and 90% of average load value at failure of 3 respective CT specimens for each treatment combination. Frequency of the test were kept low at 0.5 hz to avoid addition to the failure due to thermal failure to the specimens using a 10 kN Load cell. The data obtained from the fatigue tests was in the form of load versus stroke and number of cycles, where the number of cycles to failure was recorded, respectively. For calculating the K_{Ic} of the CT specimen in fatigue, the ASTM 5045-99 was followed. A linear elastic fracture under plain strain condition was assumed to occur in the CT specimen. However, these assumptions were confirmed using the eq. 5-7, whereas the dimensions of the CT specimen accomplish the plane strain condition. A 95% secant offset method is used as described in ASTM 5045 to find the maximum load P_Q and P_{max} shown in eq. 5. It ensures that the non-linearity in the load-displacement curve is related to the crack initiation and not due to the presence of a large plastic zone. Equations 5 and 6 ensure that the specimen is in plane strain condition while avoiding excessive plasticity in the ligaments of the specimen.

$$\frac{P_{max}}{P_Q} < 1.1 \tag{5}$$

$$0.45 < a_o/W < 0.55 \tag{6}$$

$$B,\ a_o,\ (W\text{-}a_o) < 2.5\left(\frac{K_Q}{\sigma_y}\right)^2 \tag{7}$$

Where, P_{max}= Maximum load before failure, P_Q= Trial critical load, a_o = Initial crack length,

B =Thickness, W = Width, H = Height, K_Q = Trial Fracture Toughness, and σ_y = Yield strength. The yield strength is calculated from the tensile specimen printed for the different treatment combinations and these are used to calculate the K_{Ic}. The K_{Ic} values are calculated using the eqs.

11 and 12 obtained from ASTM 5045-99, where $f\left(\frac{a_O}{W}\right)$ is the geometric function of the CT specimen.

$$f\left(\frac{a_O}{W}\right) = \frac{\left(2+\frac{a_O}{W}\right)}{\left(1-\frac{a_O}{W}\right)^{\frac{3}{2}}}\left[0.886 + 4.64\left(\frac{a_O}{W}\right) - 13.32\left(\frac{a_O}{W}\right)^2 + 14.72\left(\frac{a_O}{W}\right)^3 + 5.60\left(\frac{a_O}{W}\right)^4\right] \quad (8)$$

$$K_{Ic} = \frac{F_c}{B\sqrt{W}} f\left(\frac{a_o}{W}\right) \quad (9)$$

The increase in fracture toughness is obtained by subtracting the value of the average K_{Ic} of the three-reference specimen from the K_{Ic} of the specimen printed for the different treatment combinations.

3.3 Experimental Procedure

A full factor DOE was used to design and analysis the experiments using for five response variables: Increase in Number of Cycles to Failure and Increase in Fracture Toughness in fatigue (Mechanical properties), Decrease in Width, Increase in Thickness and Increase in Skewness (Geometric properties). To obtain a comprehensive statistical model and the factor level effects, 3 levels of nozzle height and plate thickness were chosen as summarized in Table 1. The two-way full factorial DOE was run for each combination of factors mentioned in Table 1. The experimental design included a total of 9 treatment combinations with 5 replications for Increase in Number of Cycles to Failure, Decrease in Width, Increase in Thickness and Increase in Skewness. For Increase in Fracture Toughness in fatigue 3 replications were made for the 9 treatment combinations. To avoid systematic biases the treatments were performed in a randomized order. Each part was printed separately on the Creality Ender 3 with each tensile specimen taking 68 minutes, CT specimen taking 95 minutes and specimen for geometric distortion took 32 minutes to print. In fatigue and geometric measurement specimen were printed with the brim around the base of dogbone and rectangular specimen, which were carefully removed with no further post-processing on the specimen. CT specimens were printed without any brim. After completing all the treatments, the parts were tested under a fatigue to obtain desired responses. The reference specimens were obtained with the same G-code as the treatments, using the factory-made print head assembly as provided with the Creality Ender 3. The increase in Number of Cycles to Failure and Fracture Toughness is obtained by subtracting the average value obtained for the control specimens with those of the treatment combinations.

Decrease in Width is obtained by subtracting the average value obtained for the treatment combinations with those of the control specimens, vice versa is true for Increase in Thickness and Increase in Skewness. The responses were calculated using MATLAB, Tracker and the statistical analysis was performed using SAS (SAS Institute Inc; Cary, NC).

Table 1. Nozzle height and Plate Thickness levels for the design of experiments.

Levels	Nozzle Height (mm)	Plate Thickness (mm)
1	1	2
2	1.5	5
3	2	10

Chapter 4 Results and Discussions

In this section the experimental results are presented along with DOE assumptions verification, the appropriate statistical model and the ANOVA analysis, thereafter, followed by discussion.

4.1 Increase in Number of Cycles to Failure, Increase in Fracture Toughness in fatigue, Decrease in width, Increase in Thickness and Increase in Skewness.

a) Increase in Number of Cycles to Failure

Increase in number of cycles to failure with respect to the nozzle height shown in the Figure 8, there we see that as nozzle height increases from 1mm to 2mm, a fall in the number of cycles to failure is obtained. As the nozzle height approaches 2mm, the top layer is exposed to a lower temperature profile when compared to the nozzle height of 1mm. This is also evident in the simulation done in the previous work as seen in the figure 10, [108]. In the simulation from figure 11, the temperature profile is seen on the plane, defined parallel to the surface of nozzle plate and at an offset of 0.3 mm (distance of nozzle height where the previously deposited layer is situated) from the nozzle. Here the temperature variation is shown with time at a point on the plane, as the block moves over it. Further, as nozzle height decreases from 2 mm to 1 mm the temperature on this plane increases by approximately 10 K or 10^{o}C. But for different plate thicknesses, the temperature profile remains somewhat similar at the defined plane as seen from contour plots from figure 10 and as well as from figure 11. The temperature profiles changes with change in nozzle height, it affects the bonding between the layer being deposited and the previous layer. This takes place because higher the temperature the extrudate will take longer time to fall below the glass transition temperature and at the same time increased temperature reduces the reptation time, these

factors ultimately encourages healing process. Similar observation has been seen by the other researchers [109-111]. Previous studies [93-96] have shown that when the temperature of the previous layer is maintained at a higher level, an increase in the strength is obtained due to better neck formation and reptation. This holds true for the current study; we see that the average increase in number of cycles to failure of the parts falls by more than 207 cycles as nozzle height increases from 1mm to 2mm.

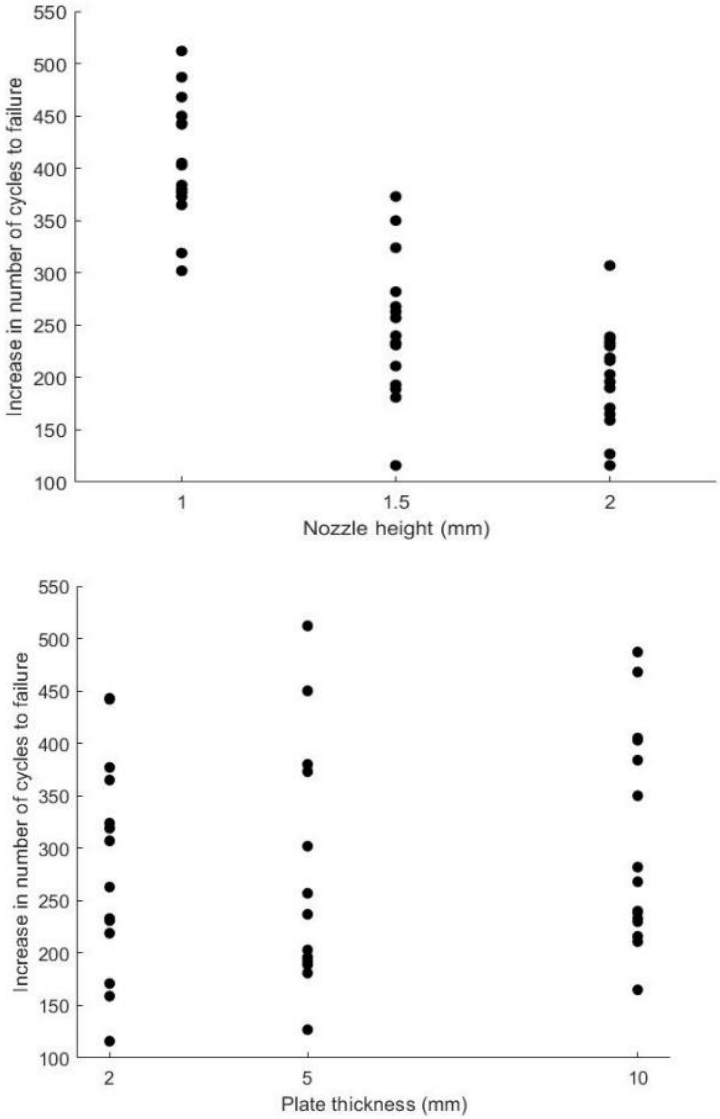

Figure 8. Plot showing increase in number of cycles to failure with respect to nozzle height and plate thickness.

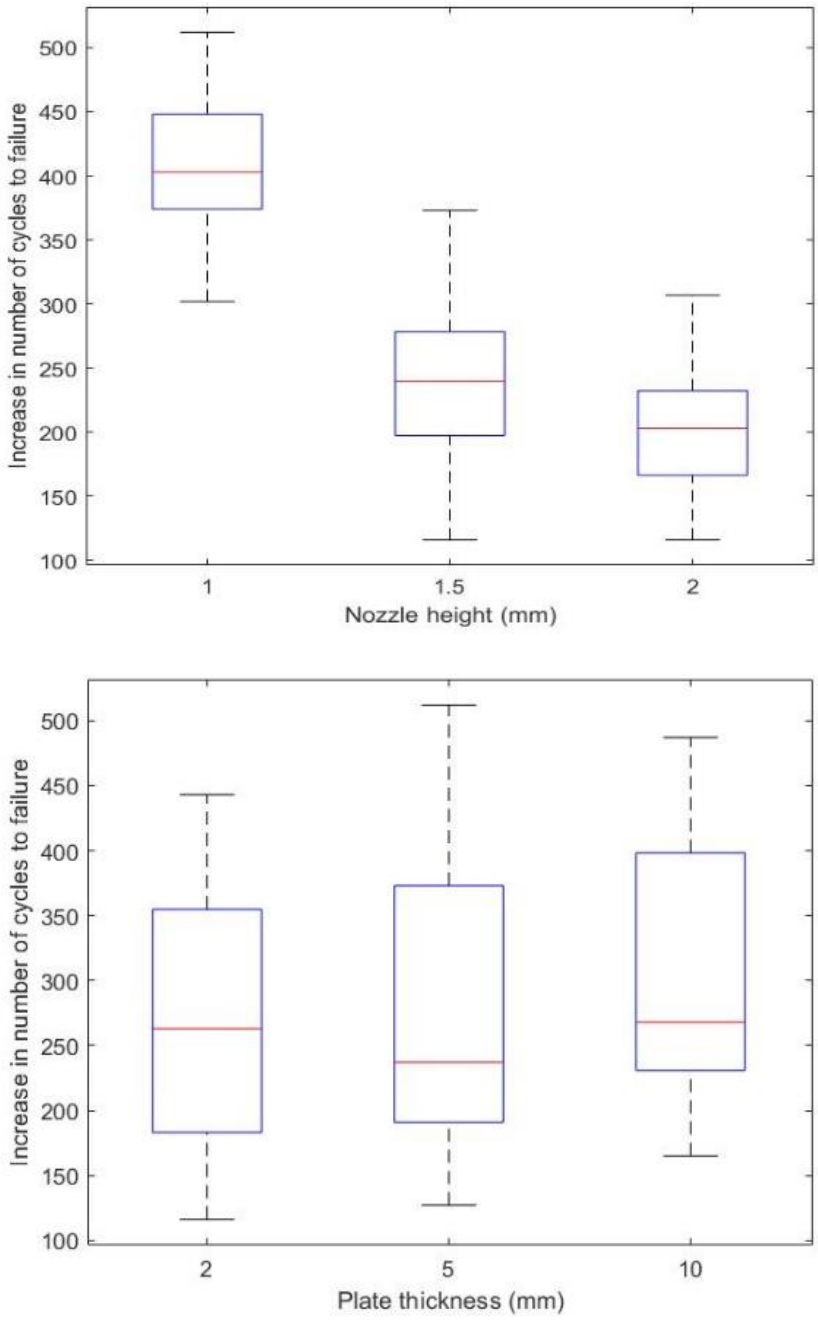

Figure 9. Boxplot plot showing variance in distribution for increase in number of cycles to failure with nozzle height and plate thickness.

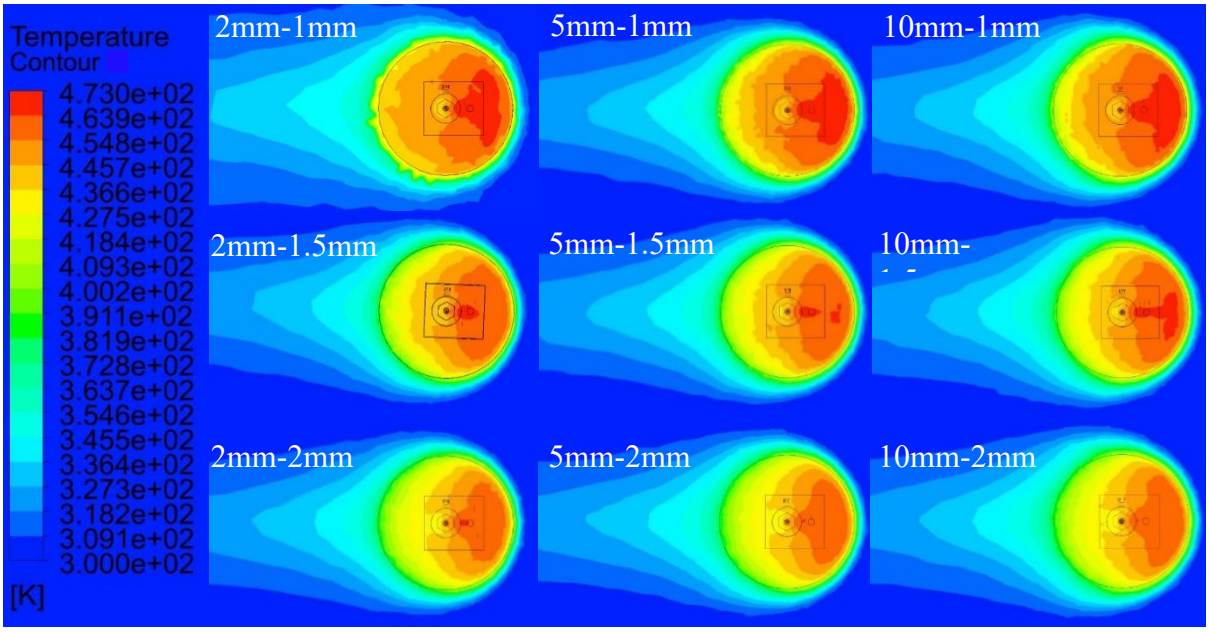

Figure 10. Simulation model showing temperature contours on a plane 0.3 mm away from the nozzle, [108].

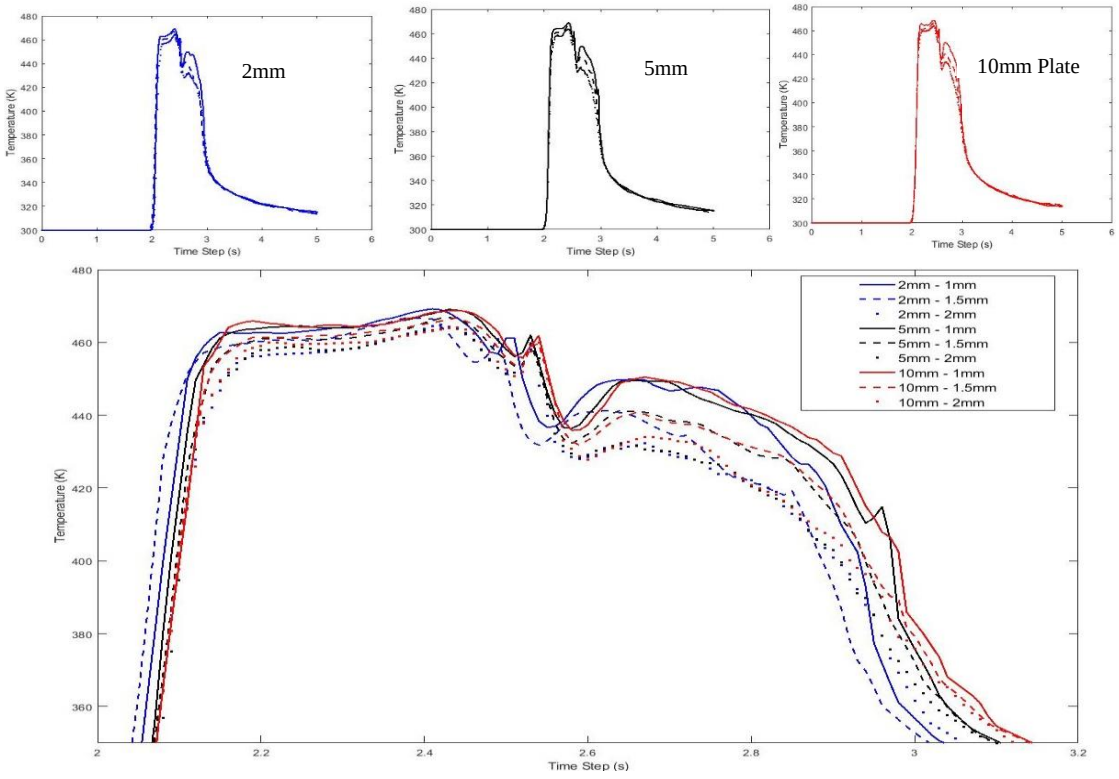

Figure 11. Temperature vs Time Step plots, [108].

On studying increase in number of cycles to failure with plate thickness as shown in figure 9, no significant difference is seen. However, the maximum increase is seen in case of 10 mm followed by 5 mm and 2 mm plate, although there is some increase, but the magnitude of the increase is trivial. When the variances from boxplots in figure 9 are compared for nozzle height and plate thickness, it is seen that the nozzle height has a dominant effect on the increase in number of cycles to failure of the parts, as compared to the plate thickness.

b) Increase in Fracture toughness (K_{Ic}) in fatigue

Increase in nozzle height exhibits a negative trend in average increase in fracture when the nozzle height increases, can be seen from figure 11. If nozzle height changes from 2mm to 1 mm the average increase in fracture toughness goes up by 15 MPa$\sqrt{mm}$ to 71 MPa$\sqrt{mm}$. It can be explained with the support of the simulation results in Figure 13, [108]. It helps in understanding the temperature distribution around the plate. If we consider a vertical line under the nozzle as shown in Figure 13, as the distance from the nozzle increases the temperature falls. This fall in temperature along a line starting 0.3 mm (layer height) below the nozzle to 15 mm has been plotted. For different nozzle heights, the temperature field changes after distance of 7 mm from the nozzle, as seen in the Figure 13 and also could be confirmed from the contour plots. This shows that for smaller nozzle heights the layers remain at a higher temperature for a longer time as compared to those with larger nozzle heights. We can see the 1mm nozzle height keeps the top surface of the printed specimen is at a much higher temperature as compared to larger nozzle heights, eventually leading to better inter layer bond formations and improved fracture toughness. From the box plots

seen in figure 12, for both nozzle height and plate thickness, it is seen that the nozzle height has much smaller spread as compared to the plate thickness showing a supreme effect of nozzle height.

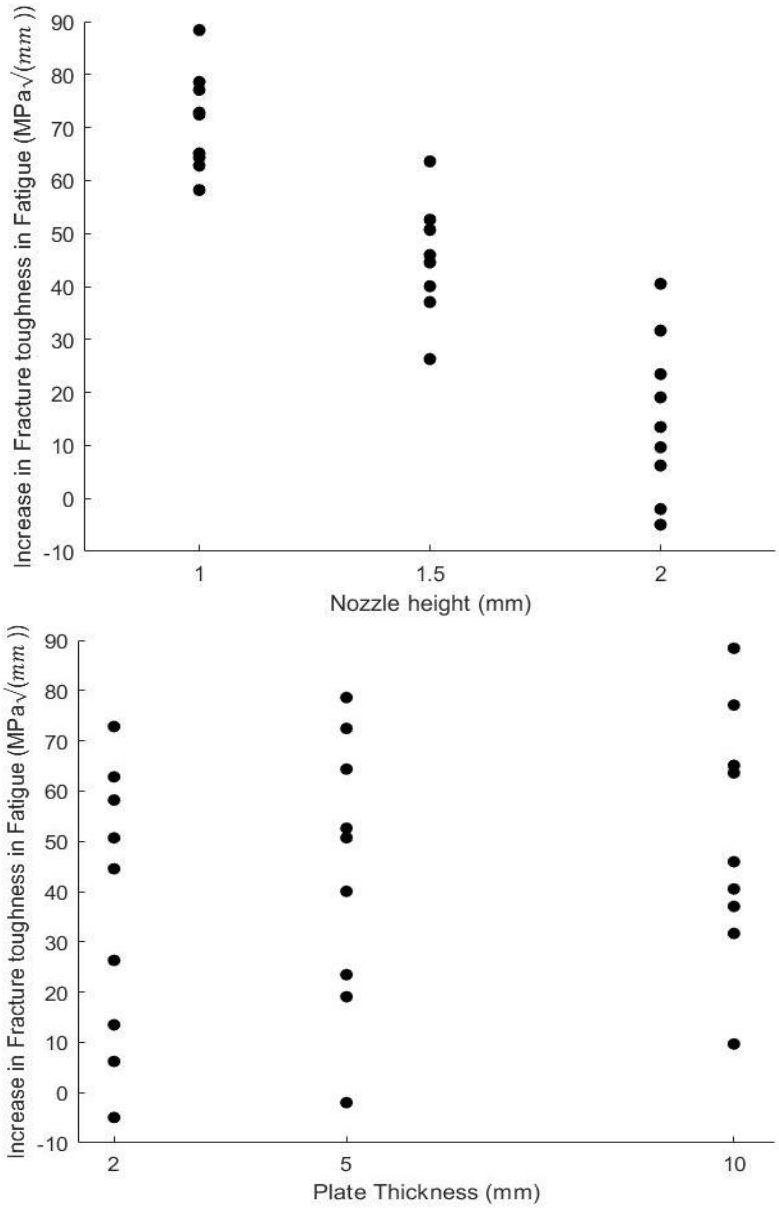

Figure 11. Plot showing increase in fracture toughness along with respect to nozzle height and plate thickness.

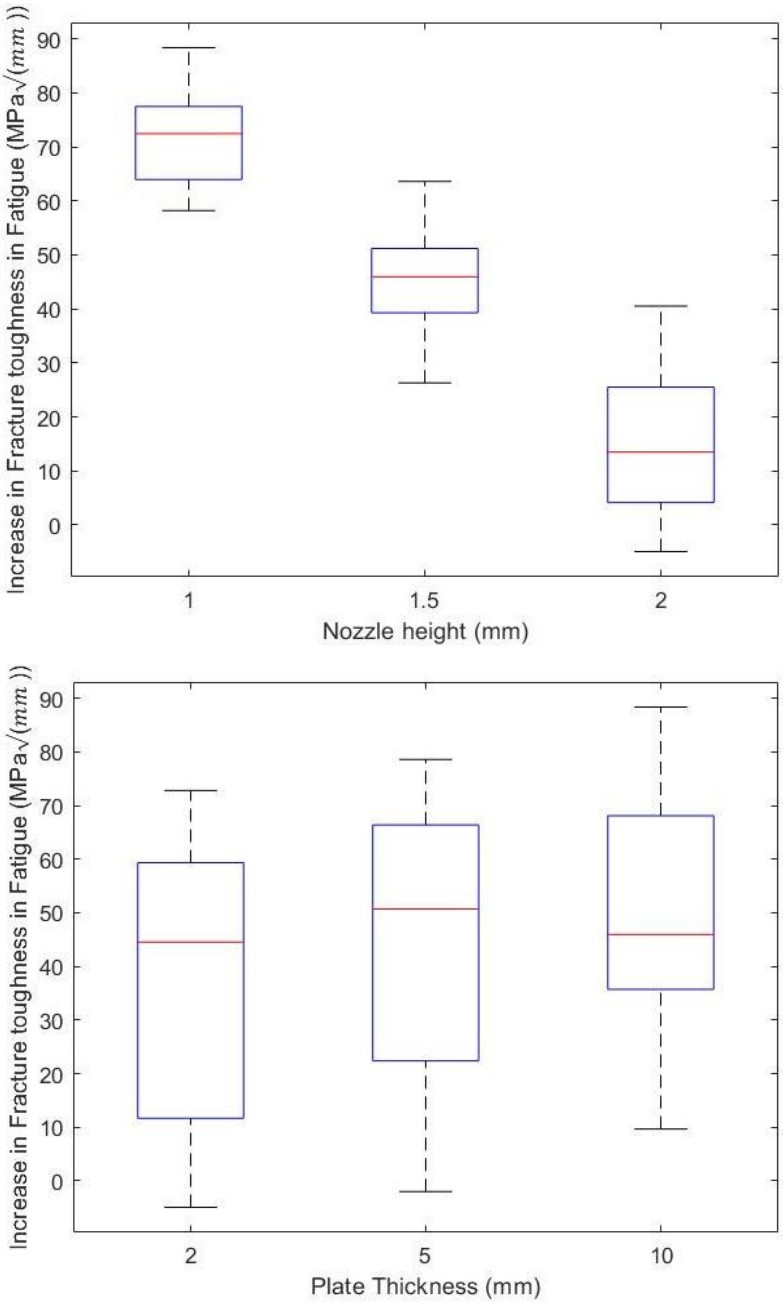

Figure 12. Boxplot plot showing variance in distribution for increase in fracture toughness with nozzle height and plate thickness.

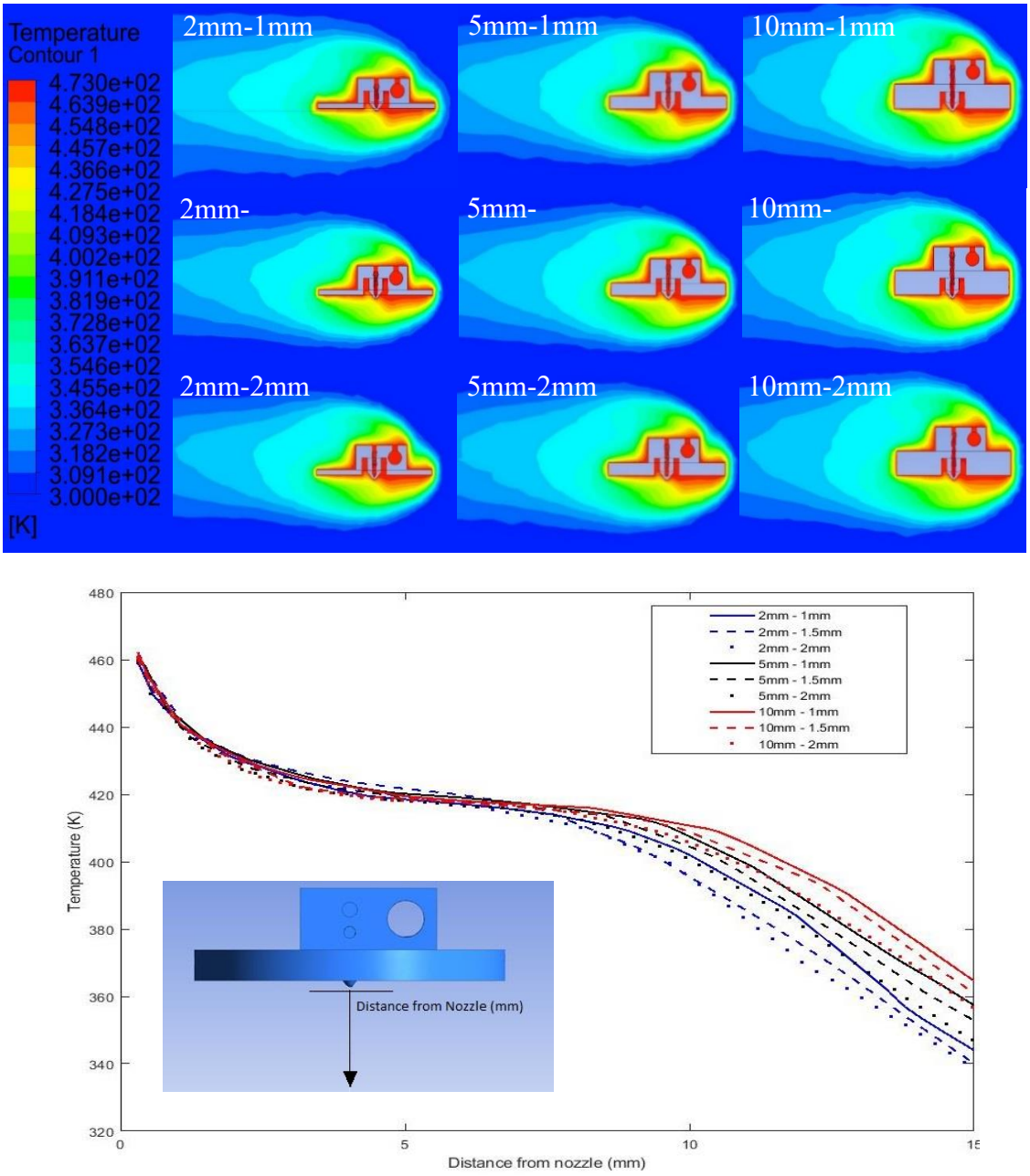

Figure 13. Simulation model showing temperature contours around the heater block, plot of temperature variation at a point moving away from the nozzle, [108].

It is seen from the plot that with respect to an increase in plate thickness a slight positive trend is seen in the average increase in fracture toughness. The fracture toughness increases from 37

MPa$\sqrt{(mm}$) to 51 MPa$\sqrt{mm}$, when plate thickness increases from the 2 mm to the 10 mm. Even from simulations it can been seen that smaller nozzle height and larger plate thicknesses keeps the layers below the nozzle at higher temperature for a longer period. It has been shown to allow for better intermingling and reptation of polymer molecules leading to improved fracture toughness in fatigue of the parts.

c) Decrease in Width, Increase in Thickness and Increase in Skewness

It is seen figure 13 that effect of nozzle height on decrease in width, increase in thickness and increase in skewness is similar to its effect on previous response variables. When the nozzle height moves from 1mm to 2mm, a dramatic fall is seen in the value of decrease in width from the reference value. The average decrease in width of the parts reduces by less than 10 % (12.04 mm to 13.18 mm) as the nozzle height increases from 1mm to 2mm. Increase in Thickness and Skewness with nozzle height of 1 mm gives an increase in average of 7.1 % and 2.9 % in thickness and skewness. Decrease in width can be correlated to higher degree of annealing across the interfaces which is influenced by the exposure temperature and time of the layers, which is significantly influenced by the nozzle height. For a nozzle height of 1mm the top layers are exposed to a much higher value of temperature as compared to the nozzle height of 2mm, thus leading to a significant fall Increase in Thickness and Skewness with increase in nozzle height. The smaller nozzle heights the layers remain at a higher temperature for a longer time as compared to those with larger nozzle heights, which induces annealing leading to more geometric distortion along the width, thickness and skewness.

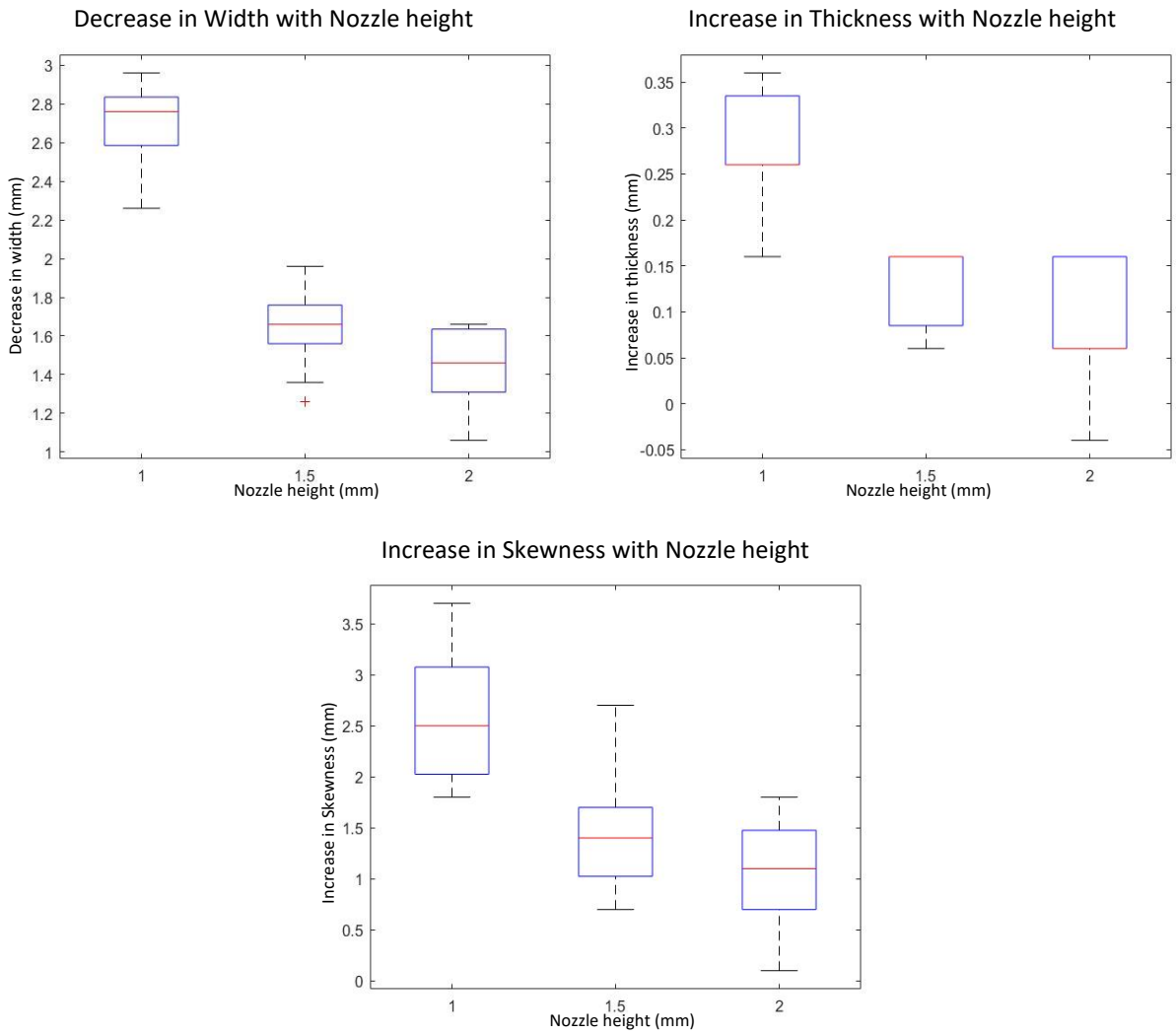

Figure 14. Box plot showing Decrease in Width, Increase in Thickness and Increase in Skewness with nozzle height.

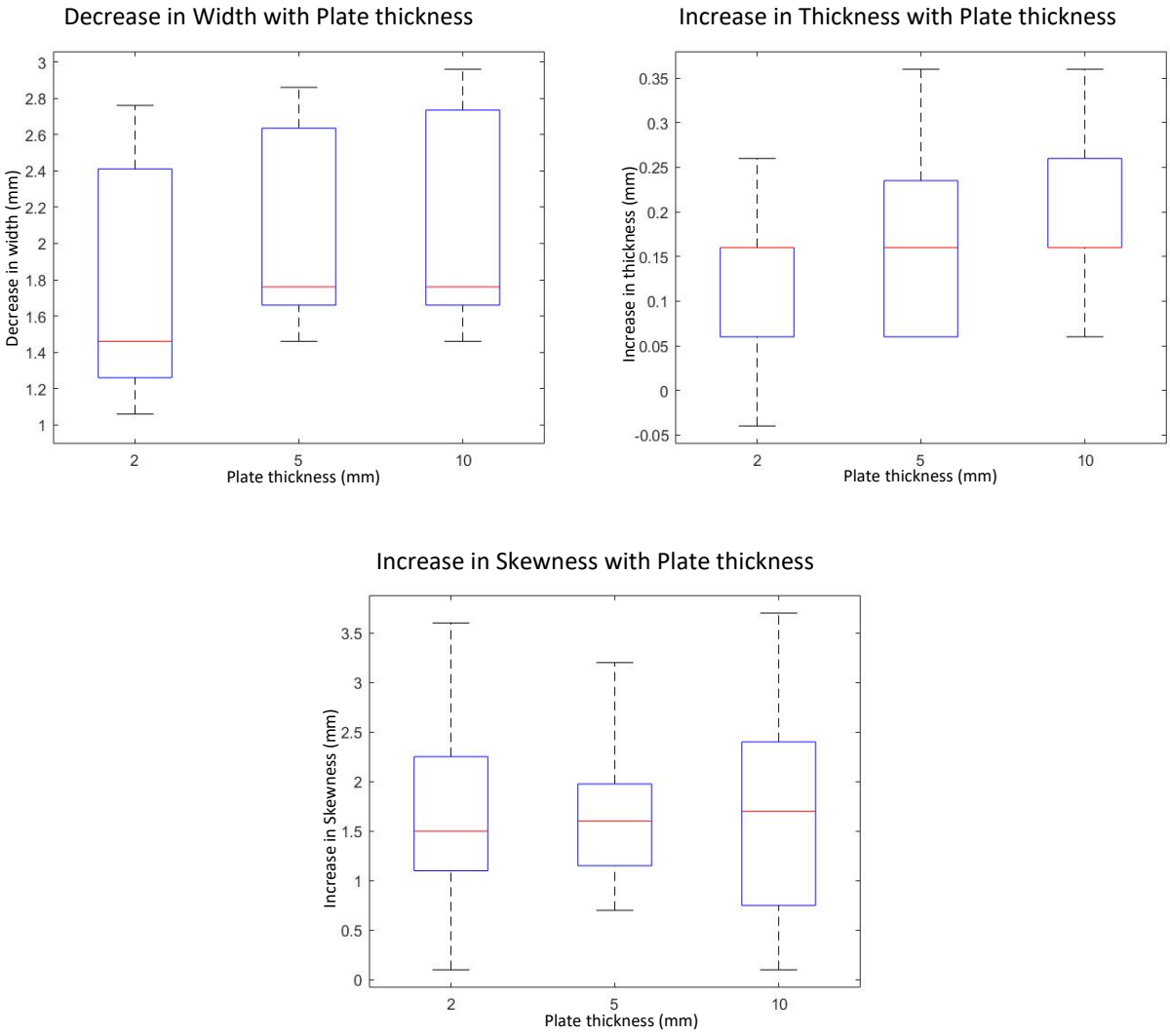

Figure 15. Box plot showing Decrease in Width, Increase in Thickness and Increase in Skewness with plate thickness.

From fig. 14 we can see the effect of plate thickness on decrease in width, increase in thickness and increase in skewness. A very slight upward trend or no obvious trend is seen in the decrease in width, increase in thickness and increase in skewness is noticed as the plate becomes thicker. As the plate thickness increases from 2mm to 10 mm the decrease in average width goes up by

2%, similar trend is seen for increase in thickness and skewness. Specially in case of skewness there is no statically significant change.

Figure 12 shows that the temperature difference between 10 mm thick plate and 2 mm thick plate at the same distance of 10 mm from the nozzle is 10 ^{o}C. Also, from the plots it can be studied that the temperature gradient is much more gradual for the 10 mm plate whereas a steeper fall is seen for the 2mm plate. Also, the boxplots shows that decrease in width, increase in thickness and increase in skewness has a larger spread for plate thickness as compared to nozzle height showing a dominant effect of the nozzle height. Also, a positive correlation is seen between increase in plate thickness with the changes in geometry whereas a negative correlation between increase in nozzle height and changes in geometry.

4.2 Influence of In-Situ annealing on void structure and it effect on mechanical properties

The improvements in mechanical properties (increase in number of cycles to failure, increase in fracture toughness in fatigue) seen, could also be explained by going through the cross-sectional images as seen in figure 15 and figure 16. The cross-sectional images of the failed surfaces of the tensile specimen for the reference and the treatment combination (10 mm-1 mm, plate thickness-nozzle height), as shown in figure 15. It can be inferred that for the reference specimen has surface with elongated voids between adjacent rasters. These elongated voids reduce the bond area and behave as failure initiation points leading to premature failure, i.e., low values of failure life and fracture toughness in the reference specimen. As we move from a nozzle height of 2mm to 1mm the voids coalesce together as shown in the figure 15. This leads to an increased bond area between layers and reduces the failure initiation zones thus increasing the increase in number of cycles to failure and increase in fracture toughness in fatigue as we reduce nozzle height to 1mm. Also, during testing of the parts crazing is noticed on the parts that are printed using the modified heater block assembly which indicates a shift from laminar behavior towards homogeneity. Also, the figure shows the changes in the void shapes and bond length. It is seen that for the reference specimen we see equally spaced diamond shaped voids but when we look at the cross-sections of the specimen on which treatment combination was used, we see that the void shape changes from diamond to a circular void. Similar changes in void shapes have been seen in previous studies with post process annealing process, supporting the observation made here in the case of in-situ annealing. These diamond shaped voids have sharp edges which act as stress concentration points leading to untimely failure of the reference specimen, but it’s transformation to circular voids, much reduces the stress intensity concentration, thus leading to a further increase in the mechanical strength of the parts in in-situ annealed parts.

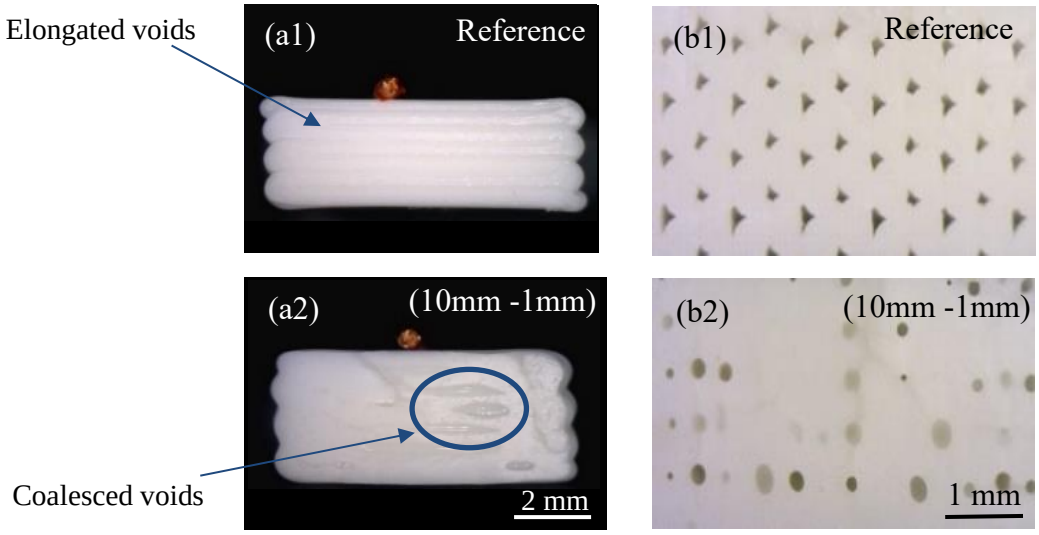

Figure 16. (a1) -(a2) failed surfaces for reference and (10mm -1mm) treatment combination; (b1) -(b2) Cross-section of a coupons printed with 10 mm block with nozzle height of 1mm, respectively; [108].

The degree of annealing increases as seen in figure 16 for decrease in nozzle height. It is very evident from the surfaces that whitening of the surface increase as the degree of annealing increases from 2 mm to 1 mm nozzle height, figure (b1-d1). Thus, it can be deduced that there is presence of polymer crazing, which becomes more prominent as the material starts moving towards a bulk material like behavior. (a3-d3), the printed parts with increasing order of annealing shows that the individual beads came closer to each other, and the bond width has gradually increased. The voids became narrower and shallow as the nozzle height decreases in compared to reference. In the 1mm nozzle height void migration takes place as seen (d1-d3), the voids have coalesced together and pinche off from tubular shaped to oval or round profile. It indicates that it is exposed to a higher temperature field as explained by the simulation results. Not only there is a

shift in the regular pattern of the voids to more random distribution from reference, but also the void coalescence to from larger voids which are also less in number.

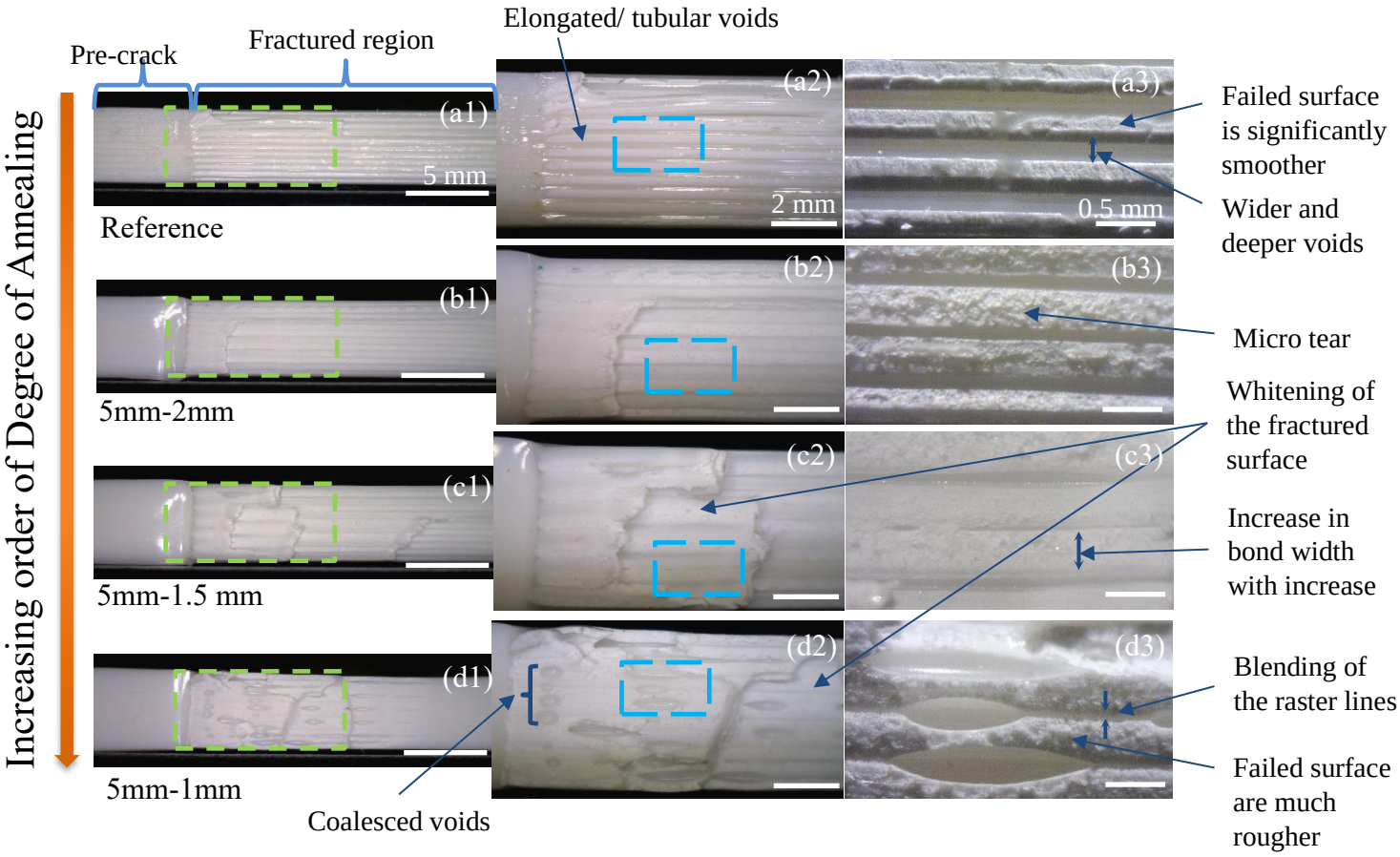

Figure 17. (a1)-(a3) Failed surface of a reference (CT) coupon, and sequential magnified images, respectively. Similarly, (b1)-(b3), (c1)-(c3) and (d1)-(f4) are representative of failed surface of a coupon printed with 5mm plate with nozzle height of 2 mm, 1.5 mm and 1 mm, and sequential magnified images, respectively.

4.3 Two-way fixed effects model and assumptions verification.

In this study for all five response variables, the two-factor full interaction model is given as,

$$Y_{ijt} = \mu_{..} + \alpha_i + \beta_j + (\alpha\beta)_{ij} + \varepsilon_{ijt} \quad (10)$$

Where the assumptions are that the model has unknown fixed effects subjected to the following restrictions:

restrictions $\sum_i (\alpha)_i = 0$, $\sum_j (\beta)_j = 0$, $\sum_i (\alpha\beta)_{ij} = 0$ and $\sum_j (\alpha\beta)_{ij} = 0$. Also, it is assumed that the error term in the ANOVA model, $\varepsilon_{ijt.}$ is normally distributed with constant variance and mutually independent errors. The assumption of normally distributed residuals is done by visually inspecting the Normal Probability Plot (NPP) for all responses as shown in Figure 17. It is seen that all plots have some sampling variations but lack of any heavy tails and no serious departures from normality. Therefore, the assumption of normality is satisfied for all the response variables. As normality is satisfied a transformation does not need to be applied to the data and we can continue with the linear model chosen in Equation 10.

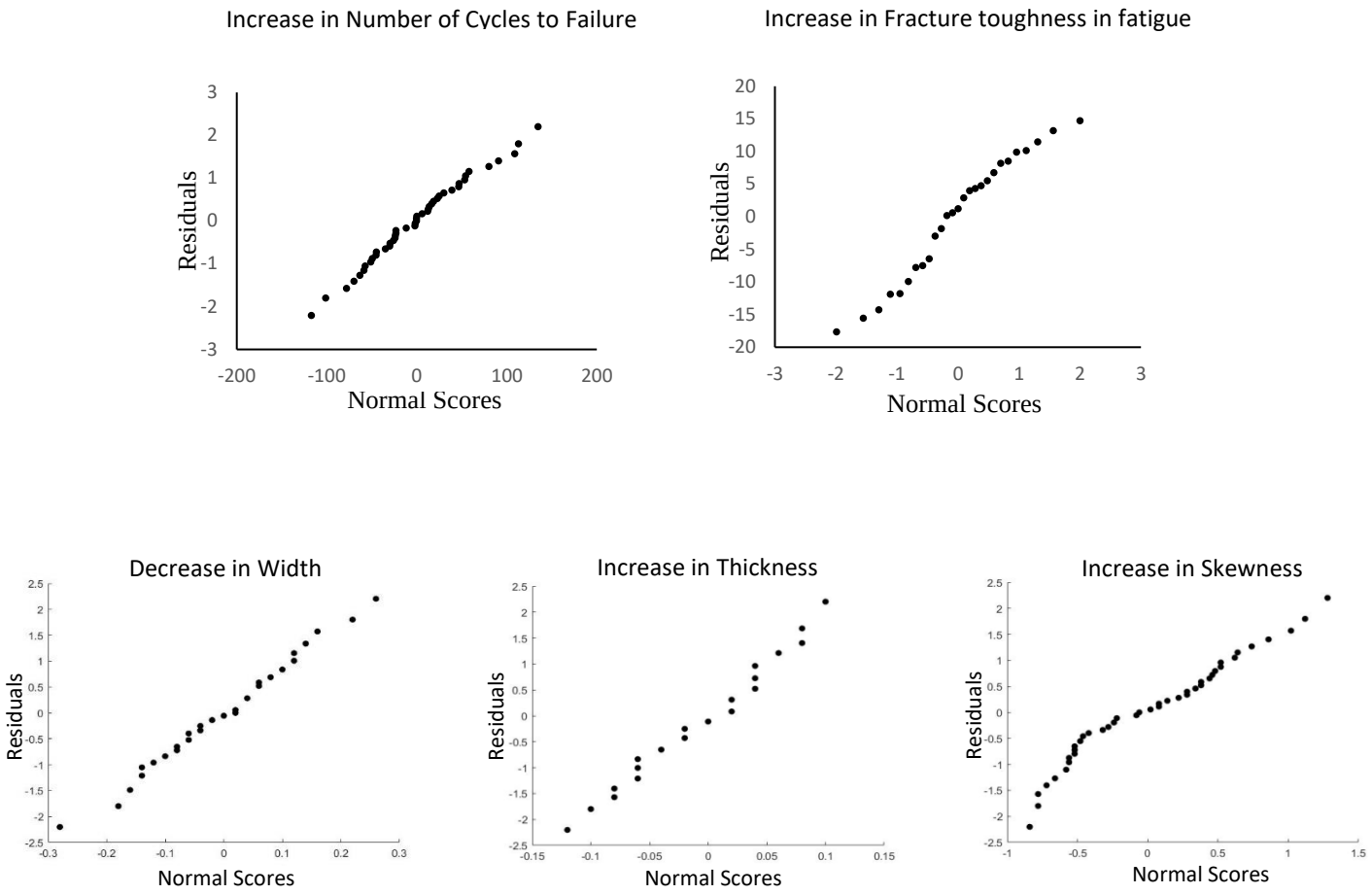

Figure 17. Normal Probability Plots for response variables.

Now the assumption of constant variance is checked. To check for this assumption the residuals are plotted as a function of fitted values (estimated means, $\hat{y}$) as shown in Figure 18. From Figure 18 for all five response variables (Increase in Number of Cycles to Failure, Increase in Fracture Toughness in fatigue, Decrease in Width, Increase in Thickness and Increase in Skewness) there are no collocated residuals, and the scatter of points are randomly distributed with somewhat equal spread. Therefore, the assumption of constant variance are satisfied.

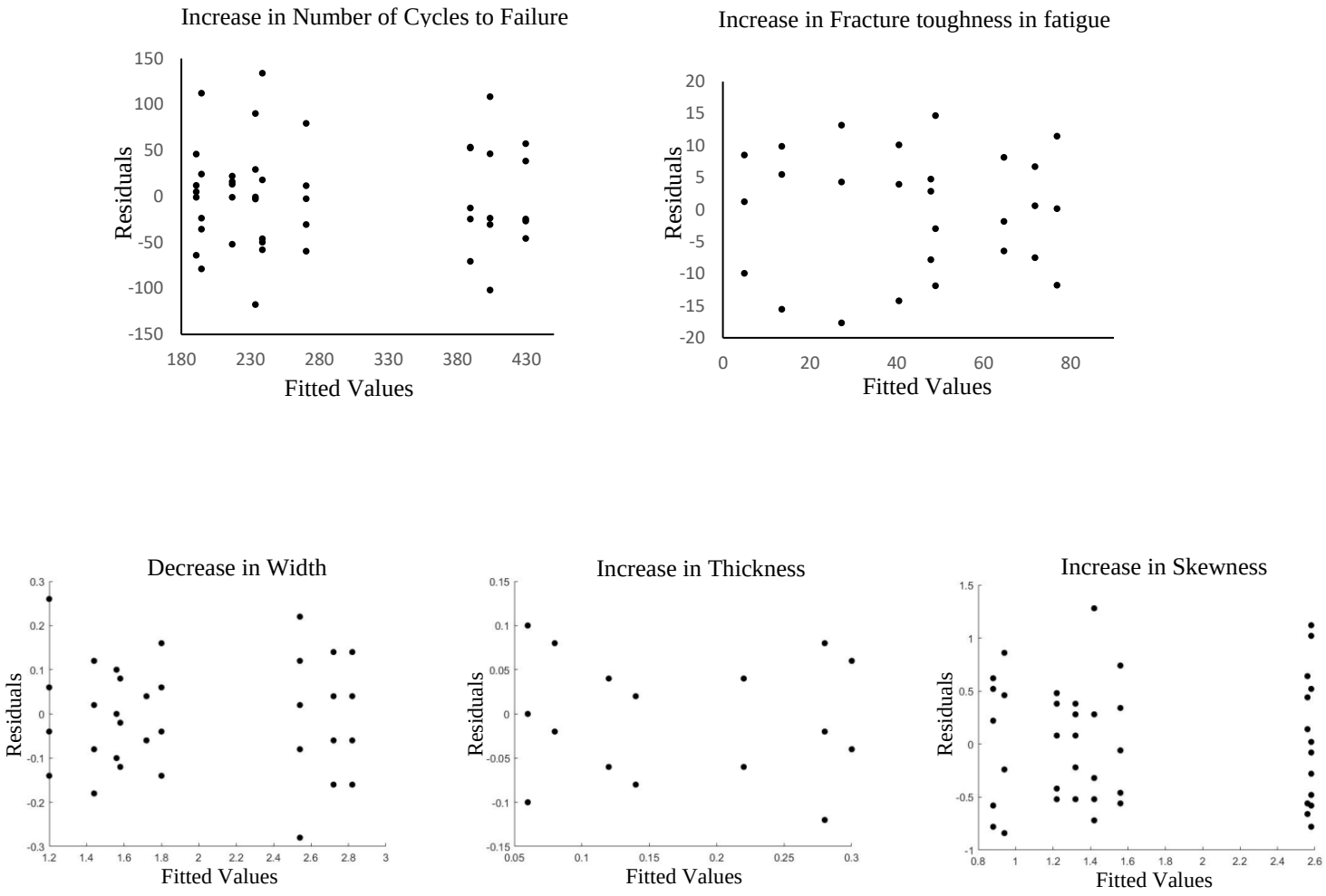

Figure 18. Residuals vs. Fitted values plots

4.4 ANOVA and Factor interactions

a) Increase in Number of Cycles to Failure

In the interaction plot from Figure 19 we see 3 distinct lines are seen which shows that the main effects for the nozzle heights are present. With the decrease in nozzle height there is significant average increase in Number of Cycles to Failure as in the case of 1 mm nozzle height we obtain maximum increase in Number of Cycles to Failure. A fall in the average increase in Number of Cycles to Failure is seen for 2mm plate thickness to 5mm plate thickness for 2mm nozzle height, but this can be attributed to the presence of sampling variability. The 3 distinct lines show a slight fall in average increase in UTS for the 5mm plate thickness plate, but the overall trend is to remain constant with zero slope thus indicating the absence of main effects due to plate thickness which can be further verified from the ANOVA results shown in Table 5.

From the ANOVA results we see the breakdown of the variability (sums of squares) of the response variable, increase in Number of Cycles to Failure. Nozzle height has the maximum contribution to the variability, and 95% of the variability in the response can be explained by the full interaction model. We check the main effects due to the plate thickness and nozzle height. The p-value for the plate thickness (0.2985) > 0.05 (0.05 significance level) , thus indicating the absence of main effects due to plate thickness at a 0.05 significance level.Again from ANOVA results we can see that, for the interaction effects, the p-value (0.9968) > 0.05 (0.05 significance level) . Thus, it can be concluded that the interaction effects are negligible too. The absence of main effects due to plate thickness and due to interaction effects on the increase in Number of Cycles to Failure shows that for future work the appropriate model is the additive model,

$$Y_{ijt} = \mu_{..} + \alpha_i + \varepsilon_{ijt} , \qquad (11)$$

that has the assumptions that $\sum_i (\alpha)_i = 0$, where α_i = main effects due to nozzle height, $\mu_{\cdot\cdot}$ = overall mean for all treatments and ε_{ijt} = error term.

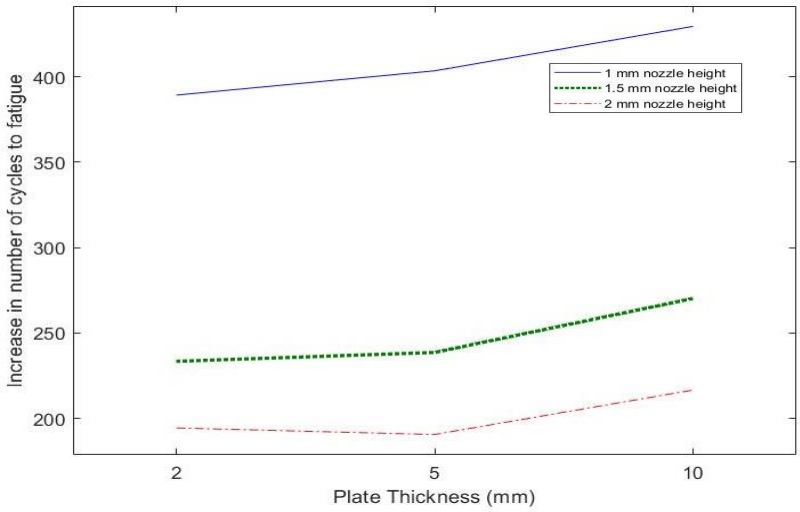

Figure 19. Interaction plot for increase in Number of Cycles to Failure.

Table3. ANOVA for the Number of Cycles to Failure

Source	Degrees of Freedom	Type III Sums of Squares	Mean Square	F value	Pr > F
Nozzle Height (h)	2	352706.98	176353.49	46.51	<.0001
Plate thickness (t)	2	9484.98	4742.49	1.25	0.2985
h × t	4	609.69	152.422	0.04	0.9968
Error	36	136512.00	3792		
Corrected Total	44	499313.64			

b) Increase in Fracture Toughness in Fatigue

In the interaction plot we can see three distinct lines referring to the different nozzle heights indicating the presence of main effects due to nozzle height. It is noticed that for an increase in nozzle height there is a significant fall in the average increase in fracture toughness in fatigue. With an increase in plate thickness the average increase in fracture toughness goes up slightly. But this trend is not consistent for the 1.5 mm nozzle height where the average increase in fracture toughness goes up from the 2mm plate thickness to the 10 mm plate thickness, but further falls from the 5mm plate to the 10 mm plate thickness.

Like the previous response variable in this case also from the ANOVA table 4, it is seen that the nozzle height has the maximum contribution to the sums of squares. Also, for the interaction effects the p- value 0.8268 > 0.05, (0.05 significance level) indicating the absence of interaction effects which was also observed from the interaction plots. The p-value for main effects due to plate thickness is seen to have marginal effect 0.0489 ~ 0.05, at a 0.05 significance level, because the p-value is just below 0.05. Thus, interaction effects are only absent, the model for future work would be an additive model as given in Equation 12 with respective assumptions.

$$Y_{ijt} = \mu_{..} + \alpha_i + \beta_j + \varepsilon_{ijt} \qquad (12)$$

with the assumptions that $\sum_i (\alpha)_i = 0$ and $\sum_j (\beta)_j = 0$, where α_i = main effects due to nozzle height, β_j = main effects due to plate thickness, $\mu_{..}$ = overall mean for all treatments and ε_{ijt} = error variable.

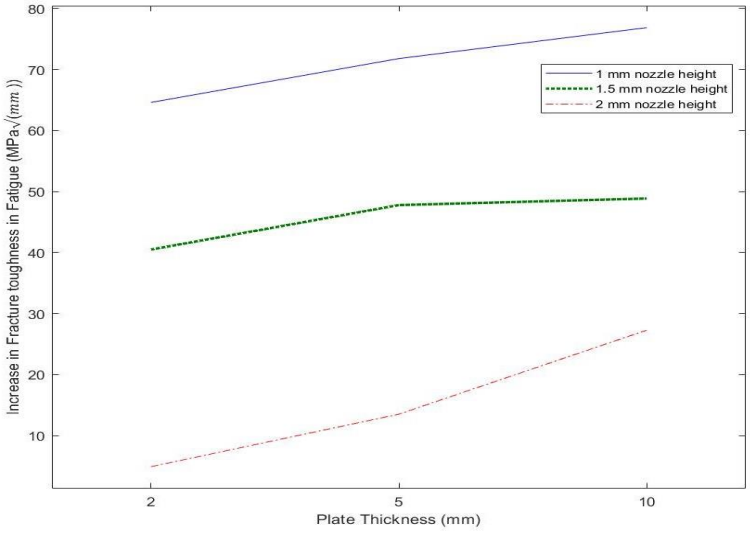

Figure 20. Interaction plot for Increase in Fracture Toughness in fatigue.

Table4. ANOVA for the Increase in Fracture Toughness in fatigue

Source	Degrees of Freedom	Type III Sums of Squares	Mean Square	F value	Pr > F
Nozzle Height (h)	2	14082.02	7041.01	54.58	<.0001
Plate thickness (t)	2	925.96	462.98	3.61	0.0482
h × t	4	190.04	47.51	0.37	0.8268
Error	36	2310.62	128.37		
Corrected Total	44	17508.64			

c) Decrease in Width, Increase in Thickness and Increase in Skewness (Geometric properties)

In the geometric distortion analysis three responses were analyzed as decrease in width, increase in thickness and increase in skewness. From the ANOVA table 5, for decrease in width, we see that p-value for nozzle height and plate thickness both are < 0.0001 (0.05 significance level), which implies that there exists main effect due to both the main factors. Unlike the

previously studied response in the current response we see a overall positive correlation of average decrease in width, with plate thickness. Similarly, when we look at the ANOVA table 6 of increase in thickness, we can conclude that there lies main effect due to nozzle height and plate thickness , since p-value for both the factors are < 0.0001 for significance level of 0.05. However, here we also see that as plate thickness increases there is a few increase in thickness in comparision to baseline replications. Thus, in the absence of interaction effects, the appropriate model is an additive model for both the response, decrease in width and increase in thickness,

$$Y_{ijt} = \mu_{..} + \alpha_i + \beta_j + \varepsilon_{ijt} \quad (13)$$

with the assumptions that $\sum_i (\alpha)_i = 0$ and $\sum_j (\beta)_j = 0$, where α_i = main effects due to nozzle height, β_j = main effects due to plate thickness, $\mu_{..}$ = overall mean for all treatments and ε_{ijt} = error variable. Finally for increase in skewness, from the ANOVA results shown in the table 7, the nozzle height has the maximum contribution to the sums of squares. We see that for the interaction effects the p-value (0.8814) > 0.05 (confidence level of 95%) confirming our observation from the table that the interaction effects are not important. Also, on comparing the p-value for the main effects due to plate thickness we see that these main effects are not present for a confidence level of 95 %. Due to the absence of main effects due to plate thickness and interaction effects, the appropriate model is as follows,

$$Y_{ijt} = \mu_{..} + \alpha_i + \varepsilon_{ijt} \quad (14)$$

with the similar assumption as in previous section.

Table 5. ANOVA for the Decrease in Width

Source	Degrees of Freedom	Type III Sums of Squares	Mean Square	F value	Pr > F
Nozzle Height (h)	2	13.3924	6.69622	427.42	<.0001
Plate thickness (t)	2	0.9618	0.48089	30.7	<.0001
h × t	4	0.0542	0.01356	0.87	0.4941
Error	36	0.564	0.01567		
Corrected Total	44	14.9724			

Table 6. ANOVA for the Increase in Thickness

Source	Degrees of Freedom	Type III Sums of Squares	Mean Square	F value	Pr > F
Nozzle Height (h)	2	0.26178	0.13089	39.27	<.0001
Plate thickness (t)	2	0.02178	0.01089	3.27	0.0497
h × t	4	0.00622	0.00156	0.47	0.7597
Error	36	0.12	0.00333		
Corrected Total	44	0.40978			

Table 7. ANOVA for the Increase in Increase in Skewness

Source	Degrees of Freedom	Type III Sums of Squares	Mean Square	F value	Pr > F
Nozzle Height (h)	2	19.548	9.774	25.09	<.0001
Plate thickness (t)	2	0.213	0.01067	0.03	0.973
h × t	4	0.4547	0.11367	0.29	0.8814
Error	36	14.024	0.38956		
Corrected Total	44	34.048			

4.5 Pairwise Comparisons.

A Tukey's pairwise comparison is done for all the the response variables to obtain the significant factor levels at a 0.05 significance level. This is an analysis of factor effects where it is recognized how the mean difference of each factor levels are statistically different from one another. For increase in number of cycles to failure as main effect due to nozzle height is present for a 95% confidence level, thus a Tukey's pairwise comparison is done for different levels of nozzle height as well as it is done for plate thickness as shown in Figure 21. However, from the previous respective data was observed there were no effect of the plate thickness, anyhow still the line plot is shown to corroborate with the result. In the figure if vertical bars are connecting two or more factor levels, it means that their mean differences are not statistically different. We see from Figure 21 that all three nozzle heights 1 mm and 1.5 mm have mean differences in the increase in number of cycles to failure that are statistically different from each other. Although the mean differences between 1.5 mm and 2 mm are not statically distinguishable. This suggests that as nozzle height is reduces from 1.5 mm to 1 mm progressively higher increases in number of cycles to failure can be achieved but between 1.5 mm and 2 mm there is no significant change. In conjunction, for the plate thickness it is seen that for a plate thickness of 2 mm, 5 mm and 10 mm the mean differences are not statistically distinguishable. Thus, best results for increase in number of cycles to failure can be achieved for a nozzle height of 1mm and plate thickness of 5 mm, where the 5 mm plate would have half the weight of the 10 mm plate and as equally effective.

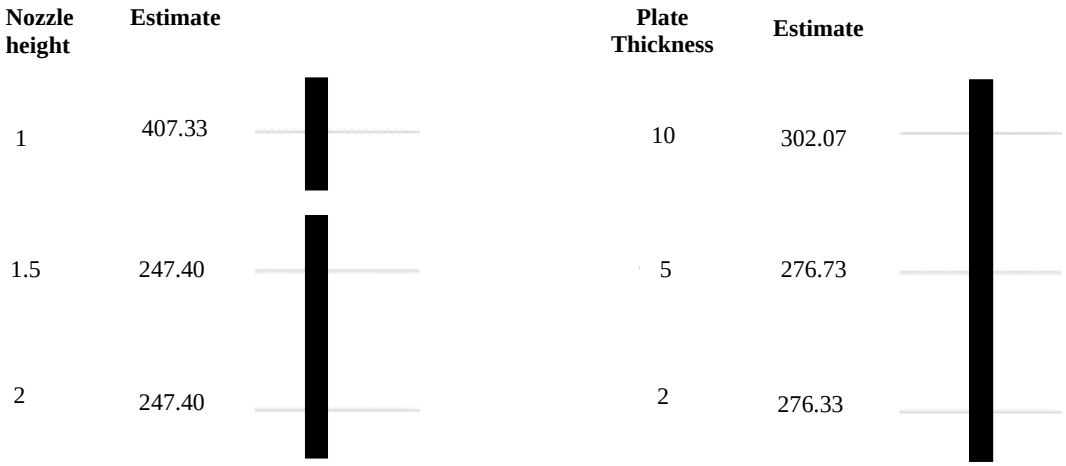

Figure 21. Line plot for Tukey's Pairwise comparison: Increase in Number of Cycles to Failure with respect to nozzle height and plate thickness

Now looking at the line plot for the increase in fracture toughness in fatigue, we can see that there are main effects due to nozzle height and to plate thickness, both. Figure 22 shows the line plots using Tukey's pairwise comparisons for the both the main effects. From the line plot meant for different nozzle heights, we see that the three levels have mean differences in increase in fracture toughness in fatigue that are statistically different from each other. This implies that as nozzle height increases from 1 mm to 1.5 mm and then to 2 mm, we get gradually see lower increase in fracture toughness. From the line plot for plate thickness, we see that the mean differences in increase in toughness for the 5 mm and 10 mm plate are not statistically different, similarly the mean differences of 5 mm and 2 mm plate are also not statistically different. Thus, maximum increase in fracture toughness in fatigue can be achieved for a 5mm plate or 10mm plate with 1mm nozzle height.

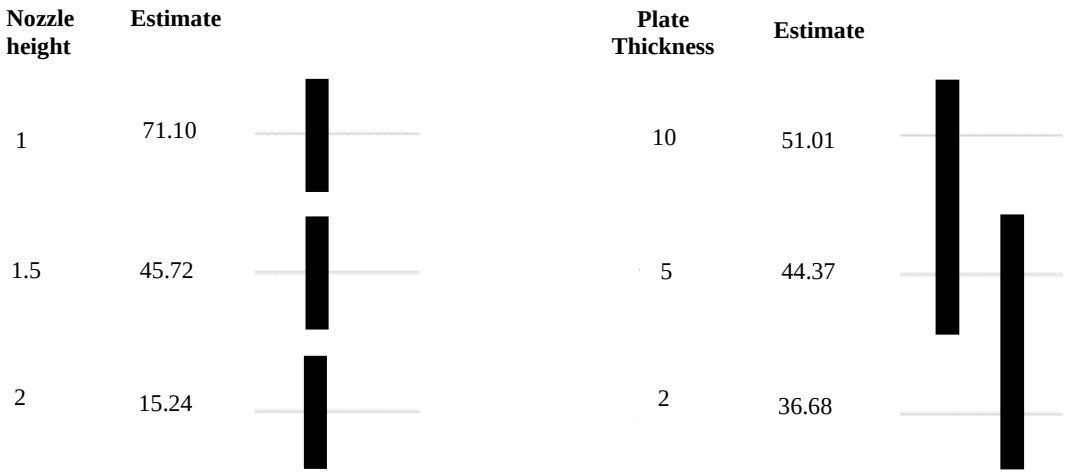

Figure 22. Line plots for Tukey's Pairwise comparison: Increase in Fracture Toughness in Fatigue with respect to nozzle height and plate thickness

Now from figure 23 shows Tukey's line plots for Decrease in Width. From the line plots for nozzle height, we see that all three nozzle heights have statistically distinguishable mean differences. It is seen that with an increase in nozzle height from 1mm to 1.5 mm to 2mm there is less increase in decrease in width the parts. From the line plots for plate thickness, the mean differences for the 5 mm and 10 mm plate thickness are not statistically distinguishable, but the mean differences for the 5 mm plate and 2 mm plate are statistically distinguishable. Thus, it can be said that for a plate thickness of 2 mm and nozzle height of 2 mm will have the least amount of decrease in width of the specimen in compared to the reference. After looking at figure 24 shows Tukey's line plots for Decrease in Thickness. We see that all three nozzle heights have statistically distinguishable mean differences. It is seen that with an increase in nozzle height from 1mm to 1.5 mm to 2mm there is less increase in decrease in width the parts. Although the mean differences between 1.5 mm and 2 mm are not statically distinguishable. This suggests that as nozzle height increases from 1 mm to

1.5 mm progressively there is less increase in thickness but between 1.5 mm and 2 mm there is no statistically significant change. And, from the line plot for plate thickness, we see that the mean differences in increase in toughness for the 5 mm and 10 mm plate are not statistically different, similarly the mean differences of 5 mm and 2 mm plate are also not statistically different. Thus, it can be said that for a plate thickness of 2 mm and nozzle height of 5 mm will treatment combination will help in minimizing the geometric distortion. Finally, from figure 25 shows Tukey's line plots for Increase in Skewness. From the line plots for nozzle height, it is very similar to the case of increase in thickness with respect to nozzle height. From the line plots for plate thickness, the mean differences for the 5 mm and 10 mm plate thickness are not statistically distinguishable, but the mean differences for the 5 mm plate and 2 mm plate are statistically distinguishable. Thus, it can be said that for a plate thickness of 2 mm and nozzle height of 2 mm will have the least skewness.

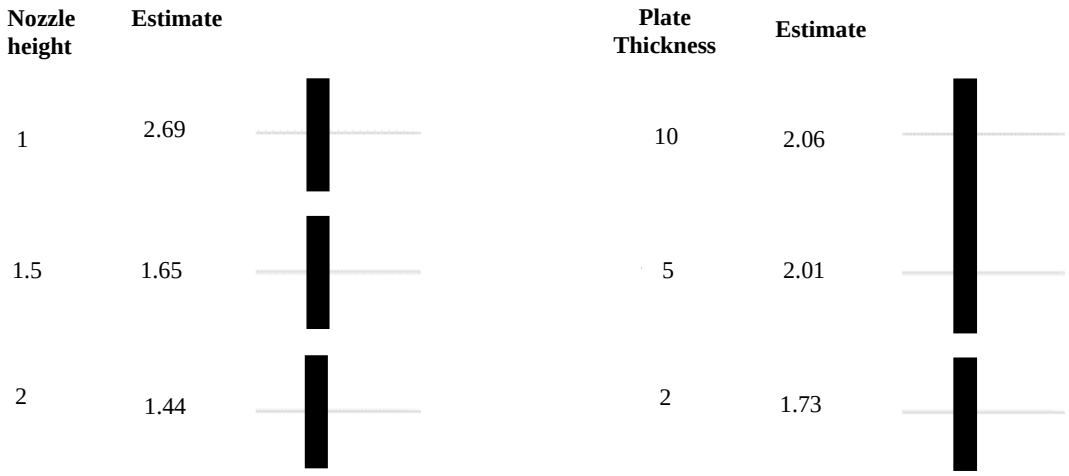

Figure 23. Line plots for Tukey's Pairwise comparison: Decrease in Width with respect to nozzle height and plate thickness

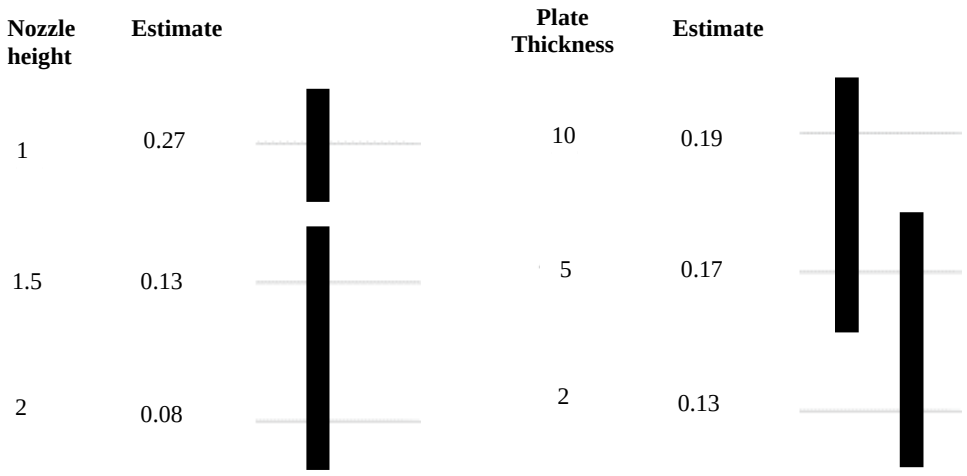

Figure 24. Line plots for Tukey's Pairwise comparison: Increase in Thickness with respect to nozzle height and plate thickness

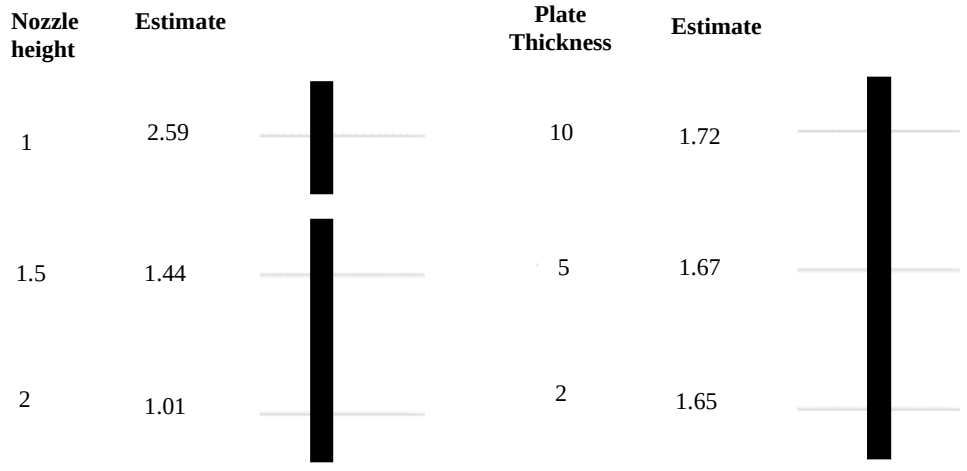

Figure 25. Line plots for Tukey's Pairwise comparison: Increase in Skewness with respect to nozzle height and plate thickness

From the above discussion is clear that how the mean differences of each factor level is different, or not, in respect to plate thickness and nozzle height. Nevertheless, it is not clear what should be the optimum treatment combination because the effect of the treatment factors on the response variables have similar orientation. This leads us to the fact that as the degree of annealing obtains better mechanical properties and more geometric distortion at the same time. Which not exactly what we are seeking for, the optimized configuration would be the case where we have significant improvement in fatigue and fracture properties but have minimized distortion along width, thickness and skewness. In next section we will look at the approach to optimized configuration.

4.6 Optimized Configuration of Novel Printhead Assembly

4.6.1 Approach to Optimized Configuration

The approach to achieve optimized case is based on the data received and its analysis. From the previous section we saw, the Tukey's pairwise comparison for maximum enhancement of mechanical strength, i.e., increase in number of cycles to failure and increase in fracture toughness were 1 mm nozzle height; this nozzle height had undoubtedly the maximum increase. The 5 mm plate thickness was chosen instead of the 10 mm plate because Tukey's pairwise comparison shows that the two are not statistically different in terms of increase in average fatigue life and fracture toughness. Thus, configuration was concluded based on the maximum increase in the desired mechanical properties but having half the weight of the nozzle 10 mm in plate thickness. Reduced weight gives reduced inertia during rapid movements due to lower mass. As well as it is seen it can reach the desired temperature in much shorter duration of time.

In contrast to the above analysis, when we look at the geometric distortion (decrease in width, increase in thickness and increase in skewness) the desired trend is opposite specially when nozzle height is of concern. The 5 mm plate thickness was chosen instead of the 2 mm plate because Tukey's pairwise comparison shows that the two are not statistically different (in terms of increase in thickness and skewness, excluding decrease in width), also the 5 mm plate is thick enough to induce the desired annealing effect to gain the improved mechanical properties. Choosing the optimum nozzle height from both the aspects keeping in consideration is trick unlike plate thickness, because for the lowest nozzle height there is the best increase in the desired mechanical properties however it is the reverse in terms of geometric properties. There is higher deviation from the reference geometry for smallest nozzle height, i.e., for 1mm.

In the figure 26 normalized values of mechanical properties is plotted against geometric properties in inverted manner, for the respective nozzle heights. These normalized values were only plotted in respect to nozzle height and not plate thickness because the variation was not significant based on the plate thickness. Similarly, the increase in skewness is omitted from the plot because it maximum average change was mere 2.9% from the baseline. From the plot we can see how the desired properties interact with each other. The interaction shows us that when the geometric distortion is given more than importance than the mechanical improvements, then on can choose the nozzle height of 1.5 mm or 2 mm. However, if superior mechanical properties are of more significance, then 1 mm nozzle height could be opted. Although, in all the tests conducted the parts were more or less under the direct influence of exposure form nozzle. This implies that if larger parts are printed then the degree of thermal annealing will go down and this leads to further reduction in geometric distortion. The change in dimension would be trivial even when the

smallest nozzle height would be chosen. Thus, for our optimized configuration from practical application perspective, the configuration chosen was 5 mm plate thickness and 1 mm nozzle height.

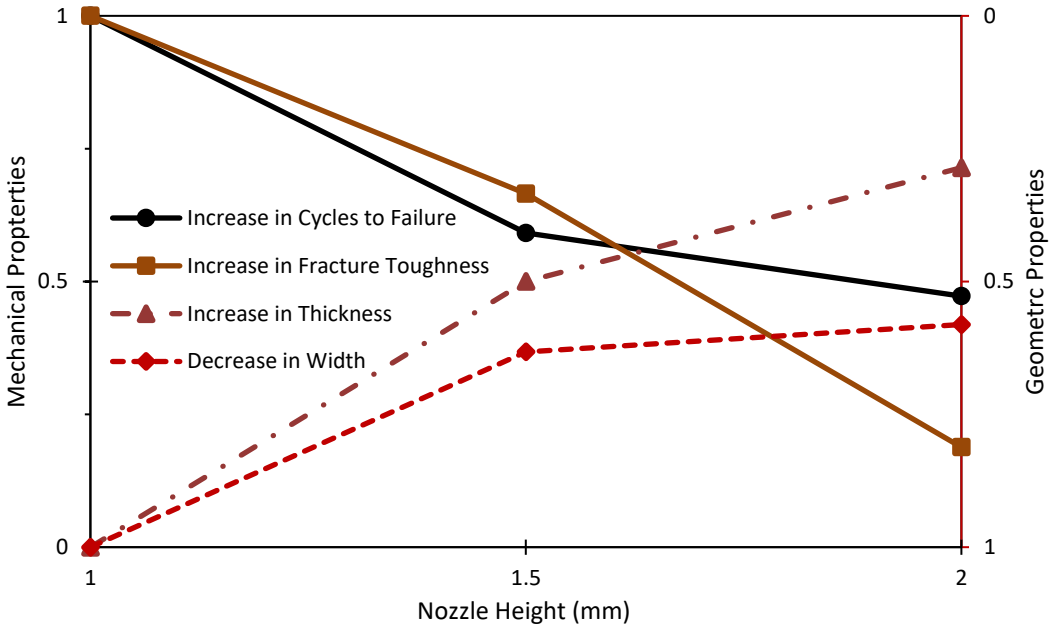

Figure 26. Normalized plot of Mechanical vs Geometric properties

4.6.2 S-N plot of Reference vs Optimized Configuration

After the optimized configuration was achieved, further this configuration was used to generate a fatigue life curve to offer bigger picture of the improvement over the existing commercial printhead. Here even for the reference case, a fatigue life cure was developed, to show the comparison between the two as seen in the figure 27. To generate the curve different load levels are needed, these load levels were taken as percentage of the average value of maximum load bared by the reference specimens. From the table 7, there are several fold increases in the fatigue life in the optimized configuration over reference. For instance, at 90 % load level there are 1029 %

increase in the number of cycles to failure. Similarly, if load level of 60 % is selected then we see 4452 % increase in fatigue life. This is substantial amount of improvement, specifically from the end user products point of view.

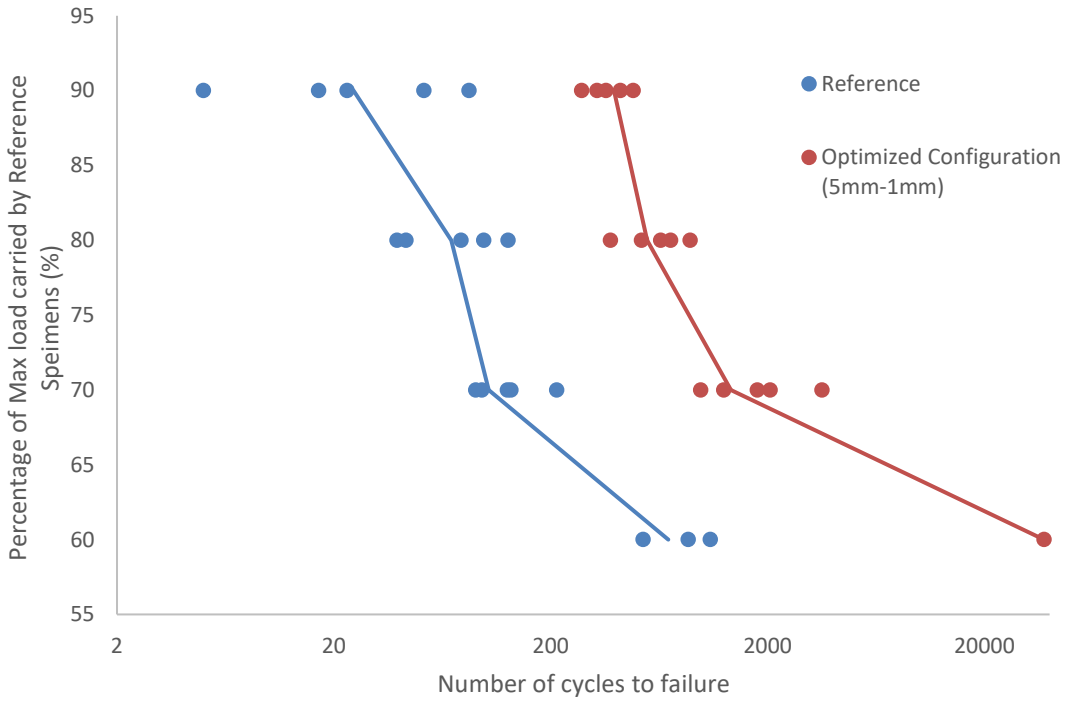

Figure 27. S-N plot of Reference vs Optimized Configuration (5mm-1mm)

Table 7. List of average values for cycles to failure for reference and optimized configuration.

Load levels (%)	Average Cycles to Failure (Reference)	Average Cycles to Failure (Optimized Configuration)	Percentage Increase (%)
90	36	406	1029
80	77	627	717
70	131	1928	1370
60	828	37688	4452

Chapter 5 Conclusion

Novel Print head Assembly was designed and optimized using Design of Experiments to characterize mechanical properties and geometric distortion of FFF parts. The DOE approach chosen helped to characterize the effect of the nozzle height and plate thickness on the five response variables, Increase in Number of Cycles to Failure, Decrease in Width, Increase in Thickness and Increase in Skewness. It is also the 2-way full factorial DOE, 3 factor levels were chosen for each, the nozzle height and plate thickness. The specimens were tested in a cyclic loading condition to obtain the number of cycles to failure and fracture toughness. The ANOVA results revealed the lack of main effect due to plate thickness and interaction effects for most of the response variables. Only main effects due to nozzle height was seen to be the most prominent for all five response variables at significance level of 0.05. Tukey's pairwise comparison was conducted to find the mean difference of each factor level for both the factors. It is seen that the smallest nozzle height, i.e., 1mm, has the maximum effect on all the responses and on the other hand the effect of different levels of plate thickness is not statically distinguishable for all the response variables. Analysis of the cross-sectional images shows that the void shape changes from diamond to circular voids, thus indicating a reduction in stress concentrations. A study of fractured surfaces shows that the failure mechanism moves from an interlaminar failure to a more homogeneous material like behavior of the in-situ annealed specimens. There were signs of improved bonding between the layers, with the presence of polymer crazing, coalescence of tubular voids into oval shaped voids and increase in bond width.

There exists trade-off between enhancement of Mechanical properties and minimizing geometric distortion; depending on the requirement, one could configure the nozzle height and

plate thickness. Optimized configuration was selected based on practical approach of achieving maximum strength improvement and less distortion while printing larger parts. Optimized factor levels for maximum increase in Fatigue failure and Fracture Toughness are: 1mm nozzle height and 5mm plate thickness. For it, an increase in number of cycles to failure by 1029 % and an increase in fracture toughness by 146.5 % was seen. Several fold improvements in fatigue life of the optimized configuration over the reference is seen; at 60 % load level there are 4452 % increase in the number of cycles to failure. From end user product manufacturing point of view, it is highly significant and proposes a print head that is effective in improving the mechanical properties, customizable to existing wide range of FFF printers and very cost effective.

Further study is required to understand the effect of the print head on large parts, where the printhead is not always on the top of the part being printed below. Also, having a mechanism integrated to the novel printhead to control the thermal exposure would be interesting as well a would provide an advantage over controlling the exposure for a fixed nozzle plate diameter and printing speed.

References

1. O. Ivanova, C. Williams, T. Campbell, Additive manufacturing (AM) and nanotechnology promises and challenges, Rapid Prototyp. J. 19 (5) (2013) 353–364, https://doi.org/10.1108/RPJ-12-2011-0127.

2. D. Dimitrov, K. Schreve, N. de Beer, Advances in three dimensional printing – state of the art and future perspectives, Rapid Prototyping J. 12 (2006) 136–147.

3. I. Zein, D.W. Hutmacher, K.C. Tan, S.H. Teoh, Fused deposition modeling of novel scaffold architectures for tissue engineering applications, Biomaterials 4 (2000) 1169–1185

4 C.M. Gonz´alez-Henríquez, M.A. Sarabia-Vallejos, J. Rodriguez-Hernandez, Polymers for additive manufacturing and 4D-printing: materials, methodologies, and biomedical applications, Prog. Polym. Sci. 94 (2019) 57–116, https://doi. org/10.1016/j.progpolymsci.2019.03.001.

5. H. Wu, W.P. Fahy, S. Kim, H. Kim, N. Zhao, L. Pilato, A. Kafi, S. Bateman, J. H. Koo, Recent developments in polymers/polymer nanocomposites for additive manufacturing, Prog. Mater. Sci. 111 (2020), 100638, https://doi.org/10.1016/j.pmatsci.2020.100638.

6. N. Turner, R. Strong, and S. A. Gold, "A review of melt extrusion additive manufacturing processes: I. Process design and modeling," Rapid Prototyping Journal, vol. 20, pp. 192-204, 2014.

7. S.A.M. Tofail, E.P. Koumoulos, A. Bandyopadhyay, S. Bose, L. O'Donoghue, C. Charitidis, Additive manufacturing: scientific and technological challenges, market uptake and opportunities, Mater. Today 21 (1) (2018) 22–37, https://doi. org/10.1016/j.mattod.2017.07.001

8. Tanikella, N.G.; Wittbrodt, B.; Pearce, J.M. Tensile strength of commercial polymer materials for fused filament fabrication 3D printing. Addit. Manuf. **2017**, 15, 40–47. [CrossRef]

9. Hill, N.; Haghi, M. Deposition direction-dependent failure criteria for fused deposition modeling polycarbonate. Rapid Prototyp. J. **2014**, 20, 221–227. [CrossRef] Materials **2019**, 12, 895 20 of 25

10. Chia, H.N.; Wu, B.M. Recent advances in 3D printing of biomaterials. J. Biol. Eng. **2015**, 9, 1–14. [CrossRef][PubMed]

11. Arif, M.F.; Kumar, S.; Varadarajan, K.M.; Cantwell,W.J. Performance of biocompatible PEEK processed by fused deposition additive manufacturing. Mater. Des. **2018**, 146, 249–259. [CrossRef]

12. Bagsik, A.; Schoppner, V. Mechanical properties of fused deposition modeling parts manufactured with ULTEM * 9085. ANTEC. **2011**, 2, 1294–1298.

13. Mireles, J.; Espalin, D.; Roberson, D.; Zinniel, B.; Medina, F.;Wicker, R. Fused Deposition Modeling of Metals.In Proceedings of the Solid Freeform Fabrication Symposium, Austin, TX, USA, 6–8 August 2012; pp. 6–8.

14. D.T. Pham, R.S. Gault, A comparison of rapid prototyping technologies, Int. J. Mach. Tools Manuf. 38 (1998) 1257–1287.

15. J.-P. Kruth, M.C. Leu, T. Nakagawa, Progress in additive manufacturing and rapid prototyping, CIRP Ann. Manuf. Technol. 2 (1998) 525–540.

16. K.V. Wong, A. Hernandez, A review of additive manufacturing, ISRN Mech. Eng. (2012) pp. 208760:1-10.

17. B. Zhang, H. Liao, C. Coddet, Effects of processing parameters on properties of selective laser melting Mg–9% Al powder mixture, Mater. Des. 34 (2012) 753–758.

18. N.K. Tolochko, M.K. Arshinov, A.V. Gusarov, V.I. Titov, T. Laoui, L. Froyen, Mechanisms of selective laser sintering and heat transfer in Ti powder, Rapid Prototyp. J. 9 (2003) 314–326.

19. I. Gibson, D. Rosen, B. Stucker, Additive Manufacturing Technologies: 3D Printing, Rapid Prototyping, and Direct Digital Manufacturing, Springer, 2014.

20. Love, L.J.; Elliott, A.M.; Post, B.K.; Smith, R.J.; Blue, C.A. The importance of carbon fiber to polymer additive manufacturing. J. Mater. Res. **2014**, 29, 1893–1898. [CrossRef]

21. Brischetto, S.; Ciano, A.; Ferro, C.G. A multipurpose modular drone with adjustable arms produced via the FDM additive manufacturing process. Curved Layer. Struct. **2016**, 3. [CrossRef]

22. Chen, H.; Yang, X.; Chen, L.; Wang, Y.; Sun, Y. Application of FDM three-dimensional printing technology in the digital manufacture of custom edentulous mandible trays. Sci. Rep. **2016**, 6, 1–6.

23. Hutmacher, D.W.; Schantz, T.; Zein, I.; Ng, K.W.; Teoh, S.H.; Tan, K.C. Mechanical properties and cell cultural response of polycaprolactone scaffolds designed and fabricated via fused deposition modeling. J. Biomed. Mater. Res. **2001**, 55, 203–216. [CrossRef]

24. Chin Ang, K.; Fai Leong, K.; Kai Chua, C.; Chandrasekaran, M. Investigation of the mechanical properties and porosity relationships in fused deposition modelling-fabricated porous structures. Rapid Prototyp. J. **2006**, 12, 100–105. [CrossRef]

25. Ravari, M.K.; Kadkhodaei, M.; Badrossamay, M.; Rezaei, R. Numerical investigation on mechanical properties of cellular lattice structures fabricated by fused deposition modeling. Int. J. Mech. Sci. **2014**, 88, 154–161. [CrossRef]

26. Tabacu, S.; Ducu, C. Experimental testing and numerical analysis of FDM multi-cell inserts and hybrid structures. Thin-Walled Struct. **2018**, 129, 197–212. [CrossRef]

27. Brischetto, S.; Ferro, C.G.; Torre, R.; Maggiore, P. 3D FDM production and mechanical behavior of polymeric sandwich specimens embedding classical and honeycomb cores. Curved Layer. Struct. **2018**, 5, 80–94. [CrossRef]

28. Arenas, L.F.; Walsh, F.C.; de León, C.P. 3D-Printing of Redox Flow Batteries for Energy Storage: A Rapid Prototype Laboratory Cell. ECS J. Solid State Sci. Technol. **2015**, 4, 3080–3085. [CrossRef]

29. Jones, R.; Haufe, P.; Sells, E.; Iravani, P.; Olliver, V.; Palmer, C.; Bowyer, A. Reprap—The replicating rapid prototype. Robotica **2011**, 29, 177–191. [CrossRef]

30. Osborn, T.; Zhou, E.; Gerzeski, R.; Mollenhauer, D.; Tandon, G.P.; Whitney, T.J.; Iarve, E.V. Experimental and theoretical evaluation of stiffness properties of fused deposition modeling parts. In Proceedings of the American Society of Composites—30th Technical Conference, East Lansing, MI, USA, 28–30 September 2015.

31. Ahn, S.H.; Montero, M.; Odell, D.; Roundy, S.; Wright, P.K. Anisotropic material properties of fused deposition modeling ABS. Rapid Prototyp. J. 2002, 8, 248–257. [CrossRef]

32. Bellini, A.; Güçeri, S. Mechanical characterization of parts fabricated using fused deposition modeling. Rapid Prototyp. J. 2003, 9, 252–264

33. C. Butler, R. McCullough, R. Pitchumani, and J. John Gillespie, "An Analysis of Mechanisms Governing Fusion Bonding of Thermoplastic Composites," Journal of Thermoplastic Composite Materials, vol. 11, pp. 338-363, 1998.

34. R. P. Wool and K. M. O'Connor, "A theory crack healing in polymers," Journal of Applied Physics, vol. 52, pp. 5953-5963, 1981.

35. F. Yang and R. Pitchumani, "Interlaminar Contact Development During Thermoplastic Fusion Bonding," Polymer Engineering and Science, vol. 42, pp. 424-438, 2002.

36. Theory of Healing at a Polymer-Polymer Interface 1115 Young Hwa Kim' and Richard P. Wool*

37. Butt, J.; Bhaskar, R. Investigating the Effects of Annealing on the Mechanical Properties of FFF-Printed Thermoplastics. *J. Manuf. Mater. Process.* **2020**, *4*, 38. https://doi.org/10.3390/jmmp4020038

38. Rodríguez, J.F.; Thomas, J.P.; Renaud, J.E. Mechanical behavior of acrylonitrile butadiene styrene (ABS) fused deposition materials. Experimental investigation. Rapid Prototyp. J. 2001, 7, 148–158. [CrossRef]

39. Cuan-Urquizo, E.; Bhaskar, A. Flexural elasticity of woodpile lattice beams. Eur. J. Mech. A Solids 2018, 67, 187–199.

40. Cuan-Urquizo, E.; Yang, S.; Bhaskar, A. Mechanical characterisation of additively manufactured material having lattice microstructure. IOP Conf. Ser. Mater. Sci. Eng. 2015, 74, 12004.

41. D. P. Cole, J. C. Riddick, H. M. Iftekhar Jaim, K. E. Strawhecker, and N. E. Zander, "Interfacial mechanical behavior of 3D printed ABS," Journal of Applied Polymer Science, vol. 133, 2016.

42. Kazem Fayazbakhsh, Mobina Movahedi, Jordan Kalman,

43. The impact of defects on tensile properties of 3D printed parts manufactured by fused filament fabrication, Materials Today Communications, Volume 18, 2019, Pages 140-148, ISSN 2352-4928, https://doi.org/10.1016/j.mtcomm.2018.12.003.

44. Rajpurohit, S.R., Dave, H.K. Analysis of tensile strength of a fused filament fabricated PLA part using an open-source 3D printer. Int J Adv Manuf Technol 101, 1525–1536 (2019). https://doi.org/10.1007/s00170-018-3047-x

45. Nagendra G. Tanikella, Ben Wittbrodt, Joshua M. Pearce, Tensile strength of commercial polymer materials for fused filament fabrication 3D printing, Additive Manufacturing, Volume 15, 2017, Pages 40-47, ISSN 2214-8604, https://doi.org/10.1016/j.addma.2017.03.005.

46. G. Percoco, F. Lavecchia, and L. M. Galantucci, "Compressive Properties of FDM Rapid Prototypes Treated with a Low Cost Chemical Finishing," Journal of Applied Sciences, Engineering and Technology, vol. 4, pp. 3838-3842, October 1, 2012.

47. A. K. Sood, R. K. Ohdar, and S. S. Mahapatra, "Experimental investigation and empirical modelling of FDM process for compressive strength improvement," Journal of Advanced Research, vol. 3, pp. 81-90, 2012

48. Panda, B.N., Bahubalendruni, M.V.A.R. & Biswal, B.B. A general regression neural network approach for the evaluation of compressive strength of FDM prototypes. Neural Comput & Applic 26, 1129–1136 (2015). https://doi.org/10.1007/s00521-014-1788-5

49. C.S. Lee, S.G. Kim, H.J. Kim, S.H. Ahn, Measurement of anisotropic compressive strength of rapid prototyping parts, Journal of Materials Processing Technology, Volumes 187–188, 2007, Pages 627-630, ISSN 0924-0136, https://doi.org/10.1016/j.jmatprotec.2006.11.095.

50. Saty Dev, Rajeev Srivastava, Experimental investigation and optimization of FDM process parameters for material and mechanical strength, Materials Today: Proceedings, Volume 26, Part 2, 2020, Pages 1995-1999, ISSN 2214-7853, https://doi.org/10.1016/j.matpr.2020.02.435.

51. J. Fonseca, I.A. Ferreira, M.F.S.F. de Moura, M. Machado, J.L. Alves, Study of the interlaminar fracture under mode I loading on FFF printed parts, Composite Structures, Volume 214, 2019, Pages 316-324, ISSN 0263-8223, https://doi.org/10.1016/j.compstruct.2019.02.005.

52. G.D. Goh, V. Dikshit, A.P. Nagalingam, G.L. Goh, S. Agarwala, S.L. Sing, J. Wei, W.Y. Yeong, Characterization of mechanical properties and fracture mode of additively manufactured carbon fiber and glass fiber reinforced thermoplastics, Materials & Design, Volume 137, 2018, Pages 79-89, ISSN 0264-1275, https://doi.org/10.1016/j.matdes.2017.10.021.

53. Li, Q.; Zhao, W.; Li, Y.; Yang, W.; Wang, G. Flexural Properties and Fracture Behavior of CF/PEEK in Orthogonal Building Orientation by FDM: Microstructure and Mechanism. Polymers 2019, 11, 656. https://doi.org/10.3390/polym11040656

54. Torrado Perez, A.R.; Roberson, D.A.; Wicker, R.B. Fracture surface analysis of 3D-printed tensile specimens of novel ABS-based materials. J. Fail. Anal. Prev. 2014, 14, 343–353.

55. Aliheidari, N.; Tripuraneni, R.; Ameli, A.; Nadimpalli, S. Fracture resistance measurement of fused deposition modeling 3D printed polymers. Polym. Test. 2017, 60, 94–101.

56. Balderrama-Armendariz, C.O.; MacDonald, E.; Espalin, D.; Cortes-Saenz, D.; Wicker, R.; Maldonado-Macias, A. Torsion analysis of the anisotropic behavior of FDM technology. Int. J. Adv. Manuf. Technol. 2018, 96, 307–317

57. Domingo-Espin, M.; Borros, S.; Agullo, N.; Garcia-Granada, A.A.; Reyes, G. Influence of building parameters on the dynamic mechanical properties of polycarbonate fused deposition modeling parts. 3D Print. Addit. Manuf. 2014, 1, 70–77

58. Mohamed, O.A.; Masood, S.H.; Bhowmik, J.L. Experimental investigation for dynamic stiffness and dimensional accuracy of FDM manufactured part using IV-Optimal response surface design. Rapid Prototyp. J. 2017, 23, 736–749.

59. Mohamed, O.A.; Masood, S.H.; Bhowmik, J.L. Experimental investigations of process parameters influence on rheological behavior and dynamic mechanical properties of FDM manufactured parts. Mater. Manuf. Process. 2016, 31, 1983–1994

60. Jami, H.; Masood, S.H.; Song, W.Q. Dynamic response of FDM made ABS parts in different part orientations. Adv. Mater. Res. 2013, 748, 291–294.

61. W. Gao, Y.B. Zhang, D. Ramanujan, K. Ramani, Y. Chen, C.B. Williams, C.C.L. Wang, Y.C. Shin, S. Zhang, P.D. Zavattieri, The status, challenges, and future of additive manufacturing in engineering, J. Technol. Comput. Aided Des. Tcad 69 (2015) 65–89.

62. A.M. Forster, Materials Testing Standards for Additive Manufacturing of Polymer Materials: State of the Art and Standards Applicability, US Department of Commerce, National Institute of Standards and Technology, 2015.

63. L. Pruitt, L. Bailey, Factors affecting near-threshold fatigue crack propagation behavior of orthopedic grade ultrahigh molecular weight polyethylene, Polymer 39 (8-9) (1998) 1545–1553.

64. J.A. Sauer, M. Hara, Effect of molecular variables on crazing and fatigue of polymers, Crazing Polym. 2 (1990) 69–118.

65. V.R. Regel and V.P. Tamuzh, Polymer Mechanics 13 (1977) 392.

66. E.H. Andrews, Fracture in Polymers, Oliver and Boyd, London (1968).

67. A.N. Gent, in Fracture, an Advanced Treatise- VII, Editor, H. Liebowitz, Academic Press, N.Y.(1972).

68. J.W.S. Hearle, Journal of Materials Science 2 (1967) 474.

69. J.W.S. Hearle and E.A. Vaughn, Rheologica Acta 9 (1970) 76.

70. Special Technical Publication No. 569, Fatigue of Composite Materials, American Society of Testing Materials (1975).

71. R.J. Crawford, P.P. Benham, Some fatigue characteristics of thermoplastics, Polymer 16 (12) (1975) 908–914.

72. R.W. Hertzberg, R.P. Vinci, J.L. Hertzberg, Deformation and Fracture Mechanics of Engineering Materials, Wiley, 2012.

73. I. Constable, J.G. Williams, D.J. Burns, Fatigue and cyclic thermal softening of thermoplastics, Arch. J. Mech. Eng. Sci. 12 (1) (1970) 20–29.

74. R.J. Crawford, P.P. Benham, Cyclic stress fatigue and thermal softening failure of a thermoplastic, J. Mater. Sci. 9 (1) (1974) 18–28.

75. J.D. Ferry, Viscoelastic Properties of Polymers, 2nd Edition, J. Wiley and Sons, N.Y. (1970).

76. W. Weibull, Fatigue Testing and Analysis of Results Elsevier, (2013).

77. J. Lee, and A. Huang, Fatigue analysis of FDM materials. Rapid Prototyp. J. 19, 291–299 (2013).

79 R.W. Hertzberg, Deformation and Fracture Mechanics of Engineering Materials, J. Wiley & Sons, N.Y. (1976).

79 S. Rabinowitz and P. Beardmore, Journal of Materials Science 9 (1974) 81.

80. J. Lee, and A. Huang, Fatigue analysis of FDM materials. Rapid Prototyp. J. 19, 291–299 (2013).

81. Saleem Hashmi, Gilmar Ferreira Batalha, Chester J. Van Tyne, Bekir Yilbas, 1.03 - Testing of Polymeric Materials, Comprehensive Materials Processing, Elsevier, 2014, Pages 35-70, ISBN 9780080965338.

82. P.G. de Gennes, Reptation of a polymer chain in the presence of fixed obstacles, J. Chem. Phys. 55 (1971) 572–579, https://doi.org/10.1063/1.1675789

83. S. Prager, M. Tirrell, The healing process at polymer–polymer interfaces, J. Chem. Phys. 75 (1981) 5194–5198, https://doi.org/10.1063/1.441871.

84. F. Yang, R. Pitchumani, Healing of thermoplastic polymers at an interface under nonisothermal conditions, Macromolecules 35 (2002) 3213–3224, https://doi.org/ 10.1021/ma010858o

85. M. Tirrell, Polymer self-diffusion in entangled systems, Rubber Chem. Technol. 57 (1984) 523–556, https://doi.org/10.5254/1.3536019. [31]

86. A. Lee, R.P. Wool, FT-IR study of orientation relaxation in uniaxially oriented monodisperse atactic polystyrenes, Macromolecules 19 (1986) 1063–1068, https:// doi.org/10.1021/ma00158a022.

87. H. Watanabe, Viscoelasticity and dynamics of entangled polymers, Prog. Polym. Sci. 24 (1999) 1253–1403, https://doi.org/10.1016/S0079-6700(99)00029-5.

88. S.F. Edwards, Dynamics of polymers in solution and melts, Polymer. 26 (1985) 163–168, https://doi.org/10.1016/0032-3861(85)90025-4.

89. D.S. Pearson, G. Ver Strate, E. von Meerwall, F.C. Schilling, Viscosity and self-diffusion coefficient of linear polyethylene, Macromolecules. 20 (1987) 1133–1141, https://doi.org/10.1021/ma00171a044.

90. Cuan-Urquizo, E., Barocio, E., Tejada-Ortigoza, V., Pipes, R.B., Rodriguez, C.A. and Roman-Flores, A., 2019. Characterization of the mechanical properties of FFF structures and materials: A review on the experimental, computational and theoretical approaches. Materials, 12(6), p.895.

91. Roy, M., Yavari, R., Zhou, C., Wodo, O. and Rao, P., 2019. Prediction and experimental validation of part thermal history in the fused filament fabrication additive manufacturing process. Journal of Manufacturing Science and Engineering, 141(12).

92. Lepoivre, A., Boyard, N., Levy, A. and Sobotka, V., 2020. Heat transfer and adhesion study for the FFF additive manufacturing process. Procedia Manufacturing, 47, pp.948-955.

93. Abinesh Kurapatti Ravi, Anagh Deshpande, Keng H. Hsu, An in-process laser localized pre-deposition heating approach to inter-layer bond strengthening in extrusion based polymer additive manufacturing, Journal of Manufacturing Processes, Volume 24, Part 1,2016,Pages 179-185,ISSN 1526-6125,https://doi.org/10.1016/j.jmapro.2016.08.007.

94. Vidya Kishore, Christine Ajinjeru, Andrzej Nycz, Brian Post, John Lindahl, Vlastimil Kunc, Chad Duty, Infrared preheating to improve interlayer strength of big area additive manufacturing (BAAM) components, Additive Manufacturing, Volume 14, 2017, Pages 7-12, ISSN 2214-8604, https://doi.org/10.1016/j.addma.2016.11.008.

95. Chin-Cheng Shih, Matthew Burnette, David Staack, Jyhwen Wang, Bruce L. Tai, Effects of cold plasma treatment on interlayer bonding strength in FFF process, Additive Manufacturing, Volume 25, 2019, Pages 104-111, ISSN 2214-8604, https://doi.org/10.1016/j.addma.2018.11.005.

96. Darshan Ravoori, Hardikkumar Prajapati, Viswajit Talluru, Ashfaq Adnan, Ankur Jain, Nozzle-integrated pre-deposition and post-deposition heating of previously deposited layers in polymer extrusion based additive manufacturing, Additive Manufacturing, Volume 28, 2019, Pages 719-726, ISSN 2214-8604, https://doi.org/10.1016/j.addma.2019.06.006.

97. Li, J. Interfacial studies on the O3 modified carbon fiber-reinforced polyamide 6 composites. *Appl. Surf. Sci.* **2008**, *255*, 2822–2824

98. Chen, L.; Zhang, X.; Wang, Y.; Osswald, T.A. Laser polishing of Cu/PLA composite parts fabricated by fused deposition modeling: Analysis of surface finish and mechanical properties.

99. Wu, W.; Jiang, J.; Jiang, H.; Liu, W.; Li, G.; Wang, B.; Tang, M.; Zhao, J. Improving bending and dynamic mechanics performance of 3D printing through ultrasonic strengthening. Mater. Lett.

100. Kevin R. Hart, Ryan M. Dunn, Jennifer M. Sietins, Clara M. Hofmeister Mock, Michael E. Mackay, Eric D. Wetzel, Increased fracture toughness of additively manufactured amorphous thermoplastics via thermal annealing, Polymer,Volume 144,2018,Pages 192-204,ISSN 0032-3861,https://doi.org/10.1016/j.polymer.2018.04.024.

101. Kevin R. Hart, Ryan M. Dunn, Eric D. Wetzel, Increased fracture toughness of additively manufactured semi-crystalline thermoplastics via thermal annealing, Polymer, Volume 211, 2020, 123091, ISSN 0032-3861, https://doi.org/10.1016/j.polymer.2020.123091.

102. Hart, K.R., Dunn, R.M. and Wetzel, E.D. (2020), Tough, Additively Manufactured Structures Fabricated with Dual-Thermoplastic Filaments. Adv. Eng. Mater., 22: 1901184. https://doi.org/10.1002/adem.201901184

103.C.B.Sweeney,B.A.Lackey,M.J.Pospisil,T.C.Achee,V.K.Hicks,A.G.Moran,B.R.Teipel,M.A.Saed,M.J.Green,Welding of 3D printed carbon nanotube polymer composites by locally induced microwave heating, Sci.Adv.3(6)(2017).

104. Durgun, I.; Ertan, R. Experimental investigation of FDM process for improvement of mechanical properties and production cost. Rapid Prototyp. J. 2014, 20, 228–235.

105. Zaldivar, R.J.; Witkin, D.B.; McLouth, T.; Patel, D.N.; Schmitt, K.; Nokes, J.P. Influence of processing and orientation print effects on the mechanical and thermal behavior of 3D-Printed ULTEM®9085 Material. Addit. Manuf. 2017, 13, 71–80.

106. Wang, C.C.; Lin, T.-W.; Hu, S.-S. Optimizing the rapid prototyping process by integrating the Taguchi method with the Gray relational analysis. Rapid Prototyp. J. 2007, 13, 304–315.

107. Panda, S.K.; Padhee, S.; Anoop Kumar, S.; Mahapatra, S.S. Optimization of fused deposition modelling (FDM) process parameters using bacterial foraging technique. Intell. Inf. Manag. 2009, 1, 89–97

108. Rane, R. (2021). Characterization and Enhancement of Mechanical Properties in Thermoplastic FFF Parts using In-Situ Annealing, [Doctoral dissertation, University of Texas, Arlington].

109. Yang, F. and Pitchumani, R., 2002. Healing of thermoplastic polymers at an interface under nonisothermal conditions. Macromolecules, 35(8), pp.3213-3224.

110. Coasey, K., Hart, K.R., Wetzel, E., Edwards, D. and Mackay, M.E., 2020. Nonisothermal welding in fused filament fabrication. Additive Manufacturing, 33, p.101140.

111. Rodriguez, J.F., Thomas, J.P. and Renaud, J.E., 2000. Characterization of the mesostructure of fused-deposition acrylonitrile-butadiene-styrene materials. Rapid Prototyping Journal.